205866

CASE WESTERN RESERVE UNIVERSITY

Ms. Corinne Dicicco
Closeout Coordinator
Department of Navy
Office of Naval Research
Chicago Regional Office
536 South Clark St., Room 208
Chicago, IL 60605-1588

August 26, 1997

Dear Ms. Dicicco,

Enclosed please find a technical report of the research conducted on a NASA grant (# NCC3-503). I am submitting it as a final technical report. Please let me know if anything else is required.

Sincerely Yours,

M. Tabib-Az

Massood Tabib-Azar
Associate Professor
Electrical Eng. and Appl. Phys. Dept.
Computer Eng. and Science Dept.
Macromolecular Science Dept.
Physics Dept.

Department of Electrical Engineering and Applied Physics

MAILING ADDRESS
Case Western Reserve University
10900 Euclid Avenue
Cleveland, Ohio 44106-7221

VISITORS AND DELIVERIES
Electrical Engineering
516 Glennan Building

Phone 216-368-
Fax 216-368-2668

EFFECT OF CRYSTAL DEFECTS ON MINORITY CARRIER DIFFUSION LENGTH IN 6H SiC MEASURED USING THE ELECTRON BEAM INDUCED CURRENT METHOD

Prof. M. Tabib-Azar

Department of Electrical Engineering and Applied Physics
CASE WESTERN RESERVE UNIVERSITY
August, 1997

EFFECT OF CRYSTAL DEFECTS ON MINORITY CARRIER DIFFUSION LENGTH IN 6H SiC MEASURED USING THE ELECTRON BEAM INDUCED CURRENT METHOD

Abstract

We report values of minority carrier diffusion length in n-type 6H SiC measured using a planar EBIC method. Values of hole diffusion length in defect free regions of n-type 6H SiC, with a doping concentration of 1.7E17 cm^{-3}, ranged from 1.46 μm to 0.68 μm.

We next introduce a novel variation of the planar method used above. This "planar mapping" technique measured diffusion length along a linescan creating a map of diffusion length versus position. This map is then overlaid onto the EBIC image of the corresponding linescan, allowing direct visualization of the effect of defects on minority carrier diffusion length. Measurements of the above n-type 6H SiC resulted in values of hole diffusion length ranging from 1.2 μm in defect free regions to below 0.1 μm at the center of large defects. In addition, measurements on p-type 6H SiC resulted in electron diffusion lengths ranging from 1.42 μm to 0.8 μm.

Table of Contents

List of Figures

List of Tables

Chapter I: Introduction

1.1 Silicon Carbide

1.1.1 Material Properties of Silicon Carbide

The compound Silicon Carbide (SiC) was first observed in the laboratory by the Swedish chemist Jons Berzelius in 1824 (Knippenberg, 1963). It was found by A.G. Acheson that this compound was 70% Si and 30% C by weight (Knippenberg, 1963). It is also the only compound that forms in the Si-C phase diagram (Yang, 1993). Silicon Carbide does not occur naturally on Earth, but has been found in meteorites (Moissan, 1905). Its has been given the name Moissanite by mineralogists.

Since its discovery, SiC has been known for its excellent mechanical properties. SiC is an extremely hard material, ranking at number 9 on the Mohs scale (Diamond=10; Topaz= 8). It also has a very high resistance to wear (Knippenberg, 1963). Because of these properties, it is no surprise that SiC was first used as a grinding and cutting material.

Other useful properties of SiC are its excellent thermal and chemical stability. SiC maintains its mechanical hardness at temperatures well over 1000^0 C (Yang, 1993). SiC does not melt at normal pressures, but sublimes at temperatures above 1800^0 C (Knippenberg, 1963). Shortly after it sublimes, SiC will dissociate into a Si and C vapor. SiC has also proven to be unreactive with most common acids and bases (Knippenberg, 1963). Strong oxidizing agents such as molten salts, fluorine gas at 300^0 C and CCl_4 at 1000^0 C are known reactants (Knippenberg, 1963).

It was A.G. Acheson who first recognized SiC would be an excellent material for grinding and cutting. He developed the first method of producing industrial grade SiC crystals (Acheson, 1892). In the Acheson method for producing SiC, a mixture of 40% coke, 50% silica, 7% sawdust, and 3% common salt is heated in an electric trough type furnace (Knippenberg, 1963). The temperature of the mixture is then brought up to approx. 2000^0 C over the course of 40-50 hours (although the actual temperature-time cycle is more complex than a simple linear ramp to 2000^0 C). Knippenberg (1963) gives a more detailed explanation of this method of SiC crystal growth. The resulting material from the Acheson method is usually small (< 1 cm^3) plate-like or rod-like crystallites.

Crystals produced by the Acheson method are the material of choice for sandpaper and saw blade tips. In fact, this process is still used to this day to produce industrial grade SiC. SiC is also widely used as a structural composite due to its mechanical and thermal stability (Yang, 1993). Due to its wide bandgap, SiC has also been investigated as a high-temperature/ high-power semiconductor (Yang, 1993).

1.1.2 Polytypism in SiC

Silicon Carbide has also been shown to exhibit a one dimensional form of polymorphism called polytypism. Polytypism means that SiC can have different ordering or stacking of its Si and C bi-layers. This allows for SiC to exhibit an almost infinite number of different structures, each with a different stacking sequence (Morkoc *et al.*, 1994).

In order to understand the structure of SiC, one must consider the close packing of hard spheres. In this scheme, atoms in the crystal are represented by hard spheres which are packed together in a regular array. For example, consider Figure 1.1. Layer A represents our basal plane of atoms. We next add layer B, placing one sphere on each triple point of layer A. Note that once we place one sphere on a triple point, the position of every other sphere in that layer is determined. Layer B sits upon exactly half of the triple points of Layer A.

For the next Layer, we are presented with a choice. We could either place the next Layer exactly on top of Layer A, which when repeated forms an ABABAB.... pattern, or we can place a new Layer C, which will line up vertically with the other 1/2 unused triple point from Layer A (see Figure 1.1). The next Layer above Layer C is then a new Layer A, which when repeated forms an ABCABCABC.... pattern. These two packing schemes form the

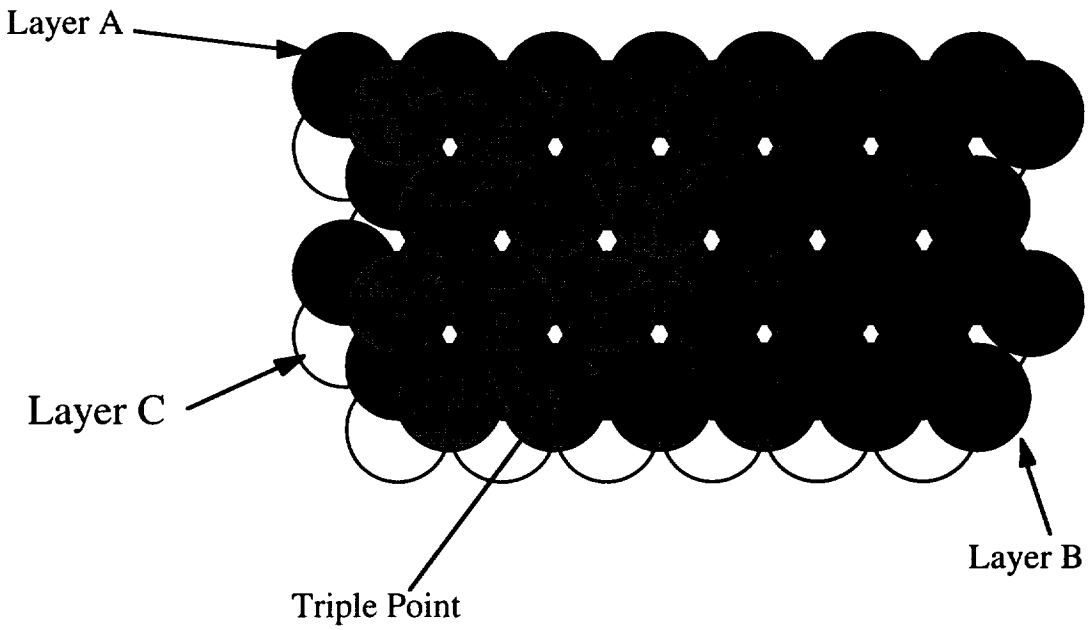

Figure 1.1 The close packing of spheres.

basis of all close pack crystal structures. It has been shown that SiC falls into this class (Yang, 1993).

In SiC the Si to C bonds form a tetrahedral geometry (Figure 1.2) (Morkoc *et al.*, 1994). As dictated by the stacking order, the bonds are either purely zinc-blende (cubic) or wurtzite (hexagonal). The zinc-blende bonds will be rotated by 60^0 to the nearest neighboring tetrahedron, while wurtzite will be a mirror image of its neighbor. Figure 1.2 depicts both bonding schemes for SiC.

In cubic structures the stacking sequence must be ABCABC... This will produce a Face Centered Cubic crystal lattice. The Diamond structure exhibited by Si is just two interwoven FCC's where the second FCC is shifted by 1/4 of the body diagonal. In SiC, one FCC Si is interwoven with a FCC C by 1/4 the body diagonal to produce the zinc-blende structure (Figure 1.2). This lone cubic polytype is referred to as 3C, 3 for the periodicity of the stacking, and C for Cubic. This polytype of SiC is also often referred to as β SiC.

In hexagonal structures, the stacking sequence is ABAB..., and all bonds are purely wurtzite. The basic hexagonal version of SiC is referred to as 2H, two for the periodicity and H for hexagonal. The family of hexagonal SiC is referred to as α SiC.

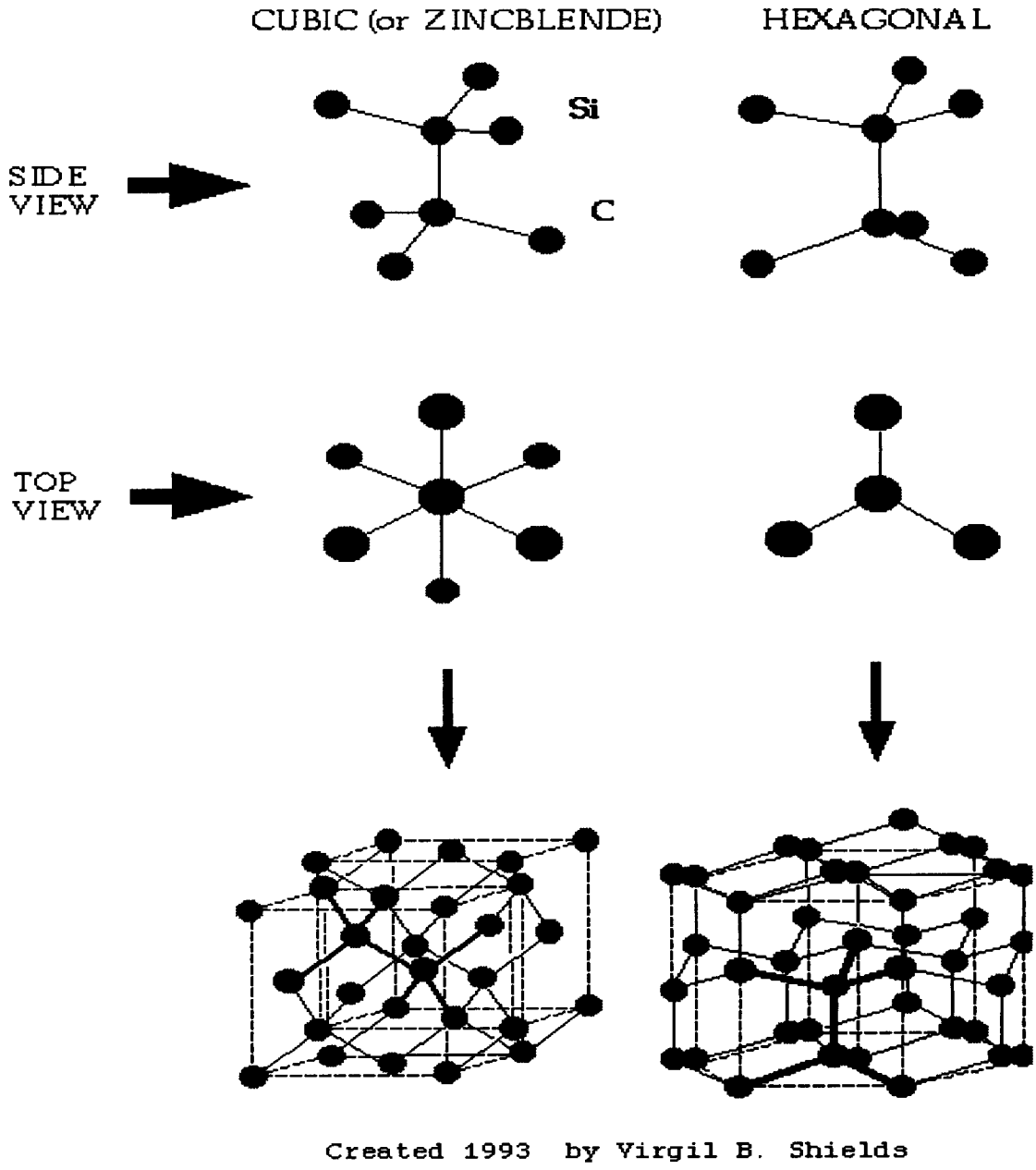

Figure 1.2 Atomic bonding in SiC. Drawing courtesy of Dr. Vergil Sheilds, Jet Propulsion Laboratory, Pasadena, CA.

More complex hexagonal structures are possible by mixing these two basic bonding schemes. For example, 4H SiC has a stacking sequence of ABCB-ABCB-ABCB.... In this polytype, half of the bonds are hexagonal, and the other half cubic, while the overall crystal structure remains hexagonal.

The SiC used in our studies was of the 6H polytype. This is the most abundant and easily formed of all the SiC polytypes (Yang, 1993). The stacking sequence of 6H SiC is ABCACB-ABCACB... In this case, two thirds of the bonds are cubic and one third are hexagonal.

Further hexagonal polytypes are possible by additional mixing of the stacking sequences. Additionally, rhombehedral structures have been shown to exist (Morkoc *et al.*, 1994). Although many polytypes of SiC are possible, the environment (temperature, pressure, etc.) in which the crystal is grown typically dictates what quantities of each polytype are produced. In most cases, large amounts of 6H are formed, with traces of 4H and 3C also present (Yang, 1993).

Although polytypism has been known to occur in SiC since 1912 (Yang, 1993), little is known of the details behind its formation. How and why different polytypes form and the mechanics of polytype transformations are questions that still have not been fully resolved (Yang, 1993; Heine *et al.,* 1991; Pirouz *et al.*, 1993; Yang, 1991).

1.1.3 SiC as a Semiconductor

Recently, the viability of Silicone Carbide as a semiconductor material has been re-evaluated. Its semiconducting properties have been known for over 30 years, but until recent advances in crystal growth, little work has been done in advancing SiC device technology.

The reason for the increased interest in developing SiC based semiconductors is the need for high-temperature, high-power, high frequency and radiation resistant electronics (Morkoc *et al.*, 1994). It is believed that a mature SiC technology could satisfy all of these needs. Unfortunately, the present state of SiC development is far from mature.

Table 1.1 summarizes the important electronic properties of SiC (Neudeck, 1997). Its wide bandgap allows SiC to be operated at much higher temperatures than either Si or GaAs. The wide bandgap ensures that SiC's background carrier concentration will remain well below the impurity concentration at elevated temperatures (Sze, 1981). A small bandgap semiconductor such as Si can be operated only up to temperatures of 250^0 C before losing its semiconducting properties (Sze, 1981).

Additionally, SiC's wide bandgap allows it to be used as an optical device in the UV region. Despite its indirect bandgap, SiC UV photodiodes and blue/UV LED's have been demonstrated (Brown *et al.*, 1993) and

	Si	GaAs	6H-SiC	4H-SiC	3C-SiC
Bandgap (eV)	1.1	1.42	3.0	3.2	2.3
Breakdown Field @ 10^{17} cm^{-3} (MV/cm)	0.6	0.6	3.2	3	> 1.5
Electron Mobility @ 10^{16} cm^{-3} (cm^2/ V-s)	1100	6000	370	800	750
Saturated Electron Drift Velocity (cm/s)	10^7	10^7	2 x 10^7	2 x 10^7	2.5 x 10^7
Thermal Conductivity (W/cm-K)	1.5	0.5	4.9	4.9	5.0
Hole Mobility @ 10^{16} cm^{-3} (cm^2/ V-s)	420	320	90	115	40
Commercial Wafers	12"	6"	1.375"	1.375"	None

Table 1.1 Electronic properties of Si, GaAs, and SiC. (Neudeck, 1997).

recently commercially produced by Cree Research. An excellent review of optical and electrical properties in SiC is given by Pensl and Choyke (1993). Although SiC has been reported to be extremely radiation hard (Itoh *et al.*, 1990; Balona *et al.*,1970; Honstvet *et al.*, 1980; Hart *et al.*, 1971; Babcock, 1965; Barry *et al.*, 1991), little work has been done to exploit this in an actual device.

Higher thermal conductivity allows SiC to remain chemically stable to much greater temperatures, well over 1000^0 C. More traditional semiconductors such as Ge and GaAs breakdown chemically at temperatures over 250^o C. In addition, SiC's high thermal conductivity allows it to dissipate the large amounts of heat generated in power applications.

The large breakdown field (5x that of Si) and saturated electron drift velocity (2x that of Si) of SiC's polytypes also make it a suitable semiconductor for high power/high frequency applications. Much of the current research in SiC is driven by the need for high power switching in the public power industry. The use of SiC could reduce the size of power devices by over 20x and allow the public power industry a 50% increase in the power carried over existing transmission lines (Neudeck, 1997). Unfortunately, large defect densities have prevented the use of SiC in commercial high power applications.

1.1.4 Bulk Crystal Growth of SiC

The Acheson process can produce acceptable industrial grade SiC, but some of the limitations in using the Acheson process to produce electronic grade SiC are:

1.) Unwanted heterojunctions. No reliable way to control which polytypes are formed. As each polytype has different electronic properties, unwanted heterojunctions are formed.

2.) Unreliable control of doping. Cannot reliably control the doping impurity density. SiC is naturally compensated n-type. It would be difficult to dope p-type using Acheson's method.

3.) Small size and large defect density. Perhaps most importantly, the Acheson process will not produce large area, defect free crystal substrates. Without these, epitaxial growth of SiC thin films must be done on a different material, where lattice mismatch begins to be of concern.

The German scientist L.A. Lely first produced single crystal SiC substrates of semiconductor grade in 1955. He used what is now called the Lely sublimation process. In this process, a graphite crucible is filled with silicon carbide powder. The powder is heated until it sublimes, forming a SiC rich vapor. As this vapor circulates around the crucible, SiC platelets form on the colder surfaces. This process is done in an inert Ar atmosphere. Impurity gases can be introduced during growth to dope the crystal. This process yields hexagonal (H) crystals of varying type, predominantly 6H, with smaller amounts 4H. Figure 1.3a shows the setup for the original Lely method. Kippenberg (1963) gives a detailed review of the early Lely process.

The Lely process could produce SiC crystals of much better purity than the Acheson process; but, was unable to produce the high purity, defect free crystals needed for commercial semiconductor manufacturing (e.g. Si crystal produced by the Czochralski method). Lely crystals were similar in size to Acheson's (much smaller than today's commercial SiC wafers), of irregular shape, had very large defect densities and often contained unwanted heterojunctions between different hexagonal polytypes (Powell, 1991). Interest in SiC waned during the 1960's and 1970's, due to the fact that no viable method (including Lely's) could be found to provide high quality electronic grade SiC.

It was the work of two Russian's, Tairov and Tsvetkov (1978;1981), in 1978 that revived the interest of the scientific community in SiC. Tairov and Tsvetkov modified Lely's original technique by including a seed crystal on which SiC would grow (Figure 1.3b). In this process, a temperature gradient

is established within the cavity so that the seed crystal is kept approx. 200° cooler than the SiC powder (Powell *et al.*, 1991). The powder is heated to temperatures over 2000° C, where the SiC sublimes as in the Lely process. The SiC vapor will crystallize when it contacts the colder seed crystal. The major advantage of this process is that the type of seed crystal will determine what type of SiC grows. Single crystal ingots of 6H and 4H SiC have been successfully grown using this method, although 3C has not yet been reported (Powell *et al.*, 1991).

This modified Lely method was further refined by Carter, Tang, and Davis (1987) (Figure 1.3c). It is now known as the "modified Lely seeded sublimation" process. This process has allowed production of large area single crystal SiC wafers (Barrett *et al.*, 1991). The defect density in these crystals is drastically lower than the older Lely platelets, but is still nowhere near the negligible defect density observed in Si substrates. The main U.S. manufacturers of SiC substrates and devices are Cree Research and Advanced Technology Materials.

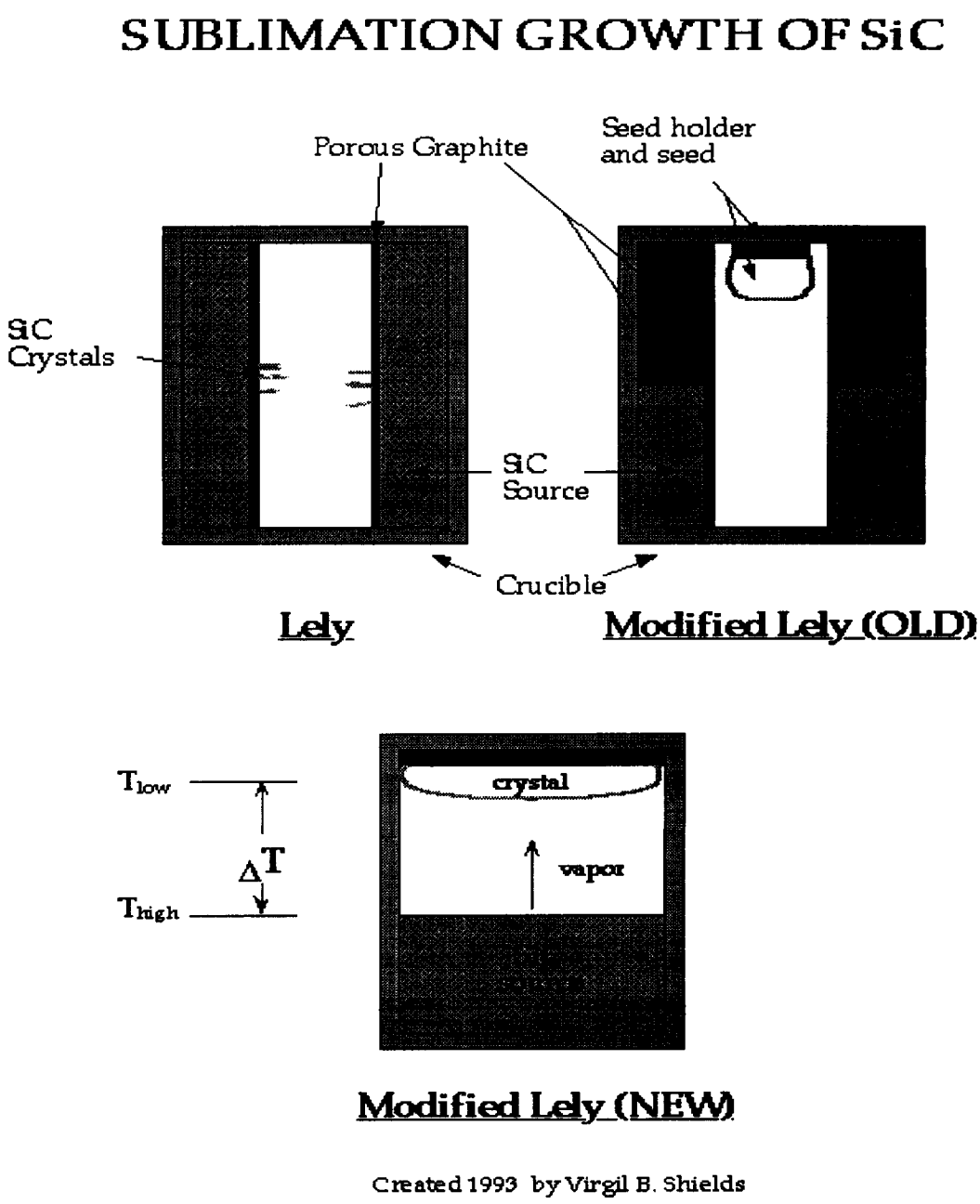

Figure 1.3 Diagrams of the original Lely sublimation process, and two new modifications. Drawing courtesy of Dr. Vergil Sheilds, Jet Propulsion Laboratory, Pasadena, CA.

1.1.5 Epitaxial Growth of SiC

Epitaxial layers can be grown from either the solid, liquid, or vapor phase of a material. Due to SiC's sublimation process, most SiC thin films are grown from the vapor phase by either Physical Vapor Deposition (PVD), Molecular Beam Epitaxy (MBE), or Chemical Vapor Deposition (CVD). All of our samples were grown using CVD, so we refer the reader to Yang (1993) for more information on MBE and PVD methods.

In Chemical Vapor Deposition, source gases are passed over a heated substrate. At this elevated temperature the gases undergo a controlled reaction, where the desired crystal is deposited on the substrate, and the byproduct gases are swept away by a constant flow of inert gas (usually H_2 or Ag). CVD is the most widely used of all the techniques used to grow commercial and research grade crystals (Yang, 1993).

In the case of SiC, most CVD systems use mixtures of silane (SiH_4) and propane (C_3H_8) or ethane (C_2H_6) in a H_2 carrier gas flow. Reactions take place at varying pressures (1 atm being the most common), varying silane to propane ratios, and at elevated temperatures. The type of substrate used (4H,6H,3C,etc.) and/or the growth conditions (i.e. temperature, ratios, pressure, etc.) will determine what polytype of SiC is formed. Small amounts of nitrogen or ammonia are introduced to dope the crystal n-type, while Al organometallics can be introduced for p-type.

One of the main problems in growing doped SiC in the past has been the problem of nitrogen compensation in the n-type SiC. Even small amounts of nitrogen in the system will dope SiC. Additionally, trying to degeneratly dope SiC produces polycrystalline growth. This prevented wide ranges of doping densities in n-type SiC and caused high levels of background donor concentration in p type SiC.

Larkin *et al.* (1994) have solved this problem using the novel technique of site-competition epitaxy. This model is based on the competition between C and N for the carbon sites in the crystal lattice, and between Si and Al for the Si sites in the lattice. Larkin was able to show that by increasing the amount of carbon source gas, the carbon atoms will "out compete" the nitrogen for lattice sites. A similar process will occur between the Si and Al, where increased concentrations of Si will "out compete" the Al for lattice sites.

This major breakthrough in SiC has allowed the production of both degeneratly doped SiC for ohmic contacts and lightly doped SiC for use in high voltage rectifiers. Using the Larkin technique, Neudeck *et al.* (1994a) was able to demonstrate the world's first 2kV SiC rectifier.

1.1.6 Defects in SiC

One of the final hurdles in developing a mature SiC technology has not been realized. This is the reduction of defects in SiC to acceptable levels. Current levels of defect densities have not allowed SiC to reach its full potential as a power semiconductor (Neudeck *et al.*, 1997).

Early work on SiC involved the heteroepitaxial growth of β SiC on Si. The 20% lattice mismatch between Si and SiC caused many interface and bulk defects (Powell *et al.*, 1991; Yang, 1993). Recently, low defect density β SiC on both Si and 6H SiC has been reported by researchers at NASA Lewis Research Center (Powell *et al.*, 1990;Neudeck *et al.*, 1993; Neudeck *et al.*, 1994b). A review of current progress in heteroepitaxy is given by Neudeck (1997) and Morkoc *et al.* (1994).

Stacking faults occur in both bulk and homoepitaxialy grown SiC (Yang, 1993). Stacking faults are a disruption in the periodicity of the stacking order. As stacking order in SiC polytypes is often complex, these faults are a common occurrence. The result of these faults are atomic dislocations within the crystal. Yang (1993) presents an excellent review of this type of defect.

Presently, the most troubling defect in bulk SiC is the micropipe defect. These defects are pipelike voids that extend through the bulk crystal. They range in diameter from the sub-micron range to a few microns (Yang, 1993). Additionally, micropipes propagate into epitaxial layers grown on the bulk substrate (Neudeck *et al.*, 1994c). The cause of these defects is still unknown, although several theories have been presented (Yang, 1993).

The presence of micropipe defects will severely limit the high voltage performance of SiC devices (Neudeck *et al.*, 1994c). At present, micropipes have limited SiC power devices to small areas and low (< 1 amp) currents (Neudeck *et al.*, 1994c). Typical defects densities are on the order of 100's of micropipes per cm^2, although recently densities as low as $5/cm^2$ have been reported (Neudeck, 1997). Cree Research has had much success in reducing defect densities, and predicts their elimination within 3-5 years (Neudeck, 1997).

1.1.7 SiC Device Technology

Many small area SiC devices are currently available on the open market. The SiC blue LED technology is fairly well developed, although high brightness and long lifetimes have not been achieved, partly due to the indirect bandgap of SiC. Other direct wide bandgap semiconductors such as GaN will most likely dominate in this future market.

Cree Research offers a variety of small area SiC power thyristors and MOSFET's, with maximum current ratings near 2 Amps. As defect density decreases, larger current rating will be possible. A complete line of high frequency and high temperature SiC devices is also offered by Cree.

The most promising aspect of SiC devices is that much of the existing Si device technology and fabrication techniques can be directly applied to SiC (Powell *et al.*, 1991). Additionally, SiC oxidizes exactly like Si forming SiO_2. This has proven to be extremely useful in the fabrication of SiC Metal-Oxide (MOS) devices. Mature SiC device technology is expected to be fully developed within the next ten years.

Based on the breakthroughs in substrate growth (modified Lely in 1987) and epitaxy (Larkin process in 1994), there has been much work done producing SiC prototype devices. Reviews of current development in SiC device technology can be found in Neudeck (1997), Morkoc *et al.* (1994), and Powell *et al.* (1991). Additionally, many papers on new SiC devices can be found in the Materials Research Society Symposium on Wide Bandgap Semiconductors edited by Moustakas *et al.* (1991) and in the Proceedings of the 5th and 6th Silicon Carbide and Related Materials Conference (Spencer *et al.*, 1993; Nakashima,1995).

1.2 The Importance of Diffusion Length

As an electron moves through a crystal lattice, recombination may occur. The recombination process involves the downward transition or "capture" of an electron in the conduction band by a lower energy state or vacancy in the valence band, referred to as a hole. The mean time an electron-hole pair (EHP) may exist until recombination occurs is referred to as the recombination lifetime. The mean distance an electron will travel before a recombination can be determined once its mobility and lifetime are known. This distance is known as the diffusion length. In an analogous situation, a hole moving in the valance band can recombine with a free electron. Therefore, both electrons and holes will have associated lifetimes and diffusion lengths.

The recombination lifetime is related to diffusion length by:

$$L \equiv \sqrt{D * \tau} \qquad (1.1)$$

where τ is the recombination lifetime and D is the diffusion coefficient given by the Einstein relation (Sze, 1981). Section 2.1 gives a more detailed account of the theory behind lifetime and diffusion length.

In a doped semiconductor, both the majority and minority carriers have associated lifetimes and diffusion lengths. The minority carrier lifetime and minority carrier diffusion length are critical device parameters. For instance, in a p-n junction, knowledge of the diffusion lengths for majority and minority carriers allow us to predict the ideal saturation current of that device. The minority carrier diffusion length is also the decay constant describing the exponential decay of minority carriers generated in a bulk semiconductor.

Of all semiconductor devices, perhaps the most important is the transistor. The transistor is a device whose behavior is dependent on its minority carrier diffusion length and recombination lifetime. For example, common emitter current gain of the transistor is directly dependent on the minority carrier lifetime in the base region. In fact, most transistor properties are dependent on either minority carrier lifetime or diffusion length. For power devices such as the thyristor, the turn off time is directly proportional to the minority carrier diffusion length.

Solar cells are another set of important devices whose properties are minority carrier dependent. The ideal conversion efficiency of a solar cell will depend on the minority carrier lifetime. Additionally, quantum efficiencies of LED's will depend on the radiative and nonradiative lifetimes, which both depend on minority carrier lifetime.

One of the most useful and time saving techniques in modern integrated circuit theory is the computer simulation of complex circuits (Sze, 1981). In order to accurately predict the response of real devices, both minority carrier lifetime and diffusion length must be known.

Diffusion length and lifetime are also indicators of a semiconductor material quality. Large amounts of defects in a material will create recombination centers. These recombination centers will reduce the local lifetimes and diffusion lengths. Large defect densities can severely limit device performance.

1.3 The Electron Beam Induced Current (EBIC) Technique and Other Methods

There are a variety of methods to measure either minority carrier diffusion length or lifetime. These methods can usually be split into two categories: photonic or electronic methods. Some of the photonic methods include photoconductive (PC) decay, photoelectromagnetic effect (PEM), photocurrent measurements, and Haynes-Shockley. The electronic methods are storage delay time and EBIC.

The above techniques associated with the measurements of minority carrier lifetime are PC, PEM, and storage delay time. Minority carrier lifetimes can also be calculated from the minority carrier mobility measured using Haynes-Shockley (Sze, 1981). Diffusion lengths are measured using EBIC or photocurrent.

In the photoconductive decay technique, often referred to as the Stevenson-Keyes (1955) method, the increase in conductivity due to minority carrier injection from a light pulse is recorded by measuring the voltage across the sample. The decay of this induced photoconductivity is a measure of the lifetime. In this method only bulk material is needed.

The photoconductive decay technique is an excellent technique for measuring longer lifetimes. This technique becomes difficult to apply to very short lifetimes, as the pulse width of the light must be much less that the lifetime. In this case, short pulse width lasers can be employed as the photogenerator, although, the limitations of the oscilloscope used to measure voltage must now be considered.

The photoelectromagnetic effect measures short circuit current across a material when a constant magnetic field is applied in a normal direction to the incoming radiation. The lifetime is approximately the square of the ratio of the short circuit current and applied magnetic field.

A third way to measure lifetime is measurement of storage delay time. This method makes use of switching transients in a pn junction diode. If a diode is suddenly switched from an on state, forward bias, to a hard off state, large reverse bias, the current will initially overshoot the diode saturation current, and remain at this larger reverse current I_r for a time t_{sd} before decaying back to the saturation current of the device. The storage delay time t_{sd} of the device occurs as the circuit dissipates the stored charge that accumulated while the device was under forward bias. It has been shown (Streetman, 1995) that this storage delay time is a simple function of the minority carrier lifetime.

The storage delay technique measures the lifetime of minority carriers in the collector region of the diode. It can only measure the bulk lifetime of the collector region, and cannot be used to measure lifetime in the emitter. For

materials with short lifetimes, the limitations of the oscilloscope must again be considered.

We can measure minority carrier mobility using the Haynes-Shockley experiment. Using this mobility and knowledge of the effective mass of minority carriers, we can calculate the lifetime (Sze, 1981). This method is dependent on knowledge of effective mass, which in newer semiconductors, may not yet be known.

In order to measure diffusion length, we can either calculate it from measured values of the lifetime and mobility using Equation 1.1, or we can measure it using photocurrrent or EBIC. In photocurrent we measure the steady state photocurrent of a junction. This photocurrent has been shown to be dependent on the absorption coefficient of the material, diffusion length, quantum yield, and physical characteristics of the device such as depletion width (Anikin *et al.*, 1992). From knowledge of the other parameters, the diffusion length is extracted. Other more complex variations of this experiment have been shown (Wu and Wittry, 1978).

In the Electron Beam Induced Current technique, diffusion length is measured using an electron beam as the radiation source. EBIC is perhaps the most widely used method to measure diffusion length, due to ease of use and its improved resolution over photocurrent. The EBIC technique, unlike the previous techniques, is uniquely suited to measure the short lifetimes and diffusion length associated with SiC. EBIC was employed to measure diffusion length in all of our experiments.

There are a number of different experimental setups used in EBIC, although the basic operating principle remains the same. A semiconductor with some type of electrical junction (either p-n or Schottky) is bombarded with an electron beam, usually from a Scanning Electron Microscope (SEM). Electron-hole pairs (EHP) are created within the bulk semiconductor upon electron bombardment (Leamy, 1982). The excess minority carriers created by the beam will begin to diffuse toward the device junction where they are collected by the built in electric field. These carriers will either "make it" to the junction or recombine in the bulk before that point depending on the diffusion length.

The device is usually connected to a current meter which measures the collected current, I_{cc}. From a knowledge of collected current versus spatial distance from the junction, the diffusion length is extracted. The equations governing charge collection for our technique will be discussed in Section 2.

The experimental setup for EBIC can be done in a number of ways. Figure 1.4 shows the various EBIC setups. In Figure 1.4 a) and c), the incident electron beam is parallel to the junction. As we scan away from the junction, the EBIC current will decrease due to a decrease in carriers diffusing to the junction before recombination. If we neglect surface recombination velocity (SRV), the current follows a simple exponential

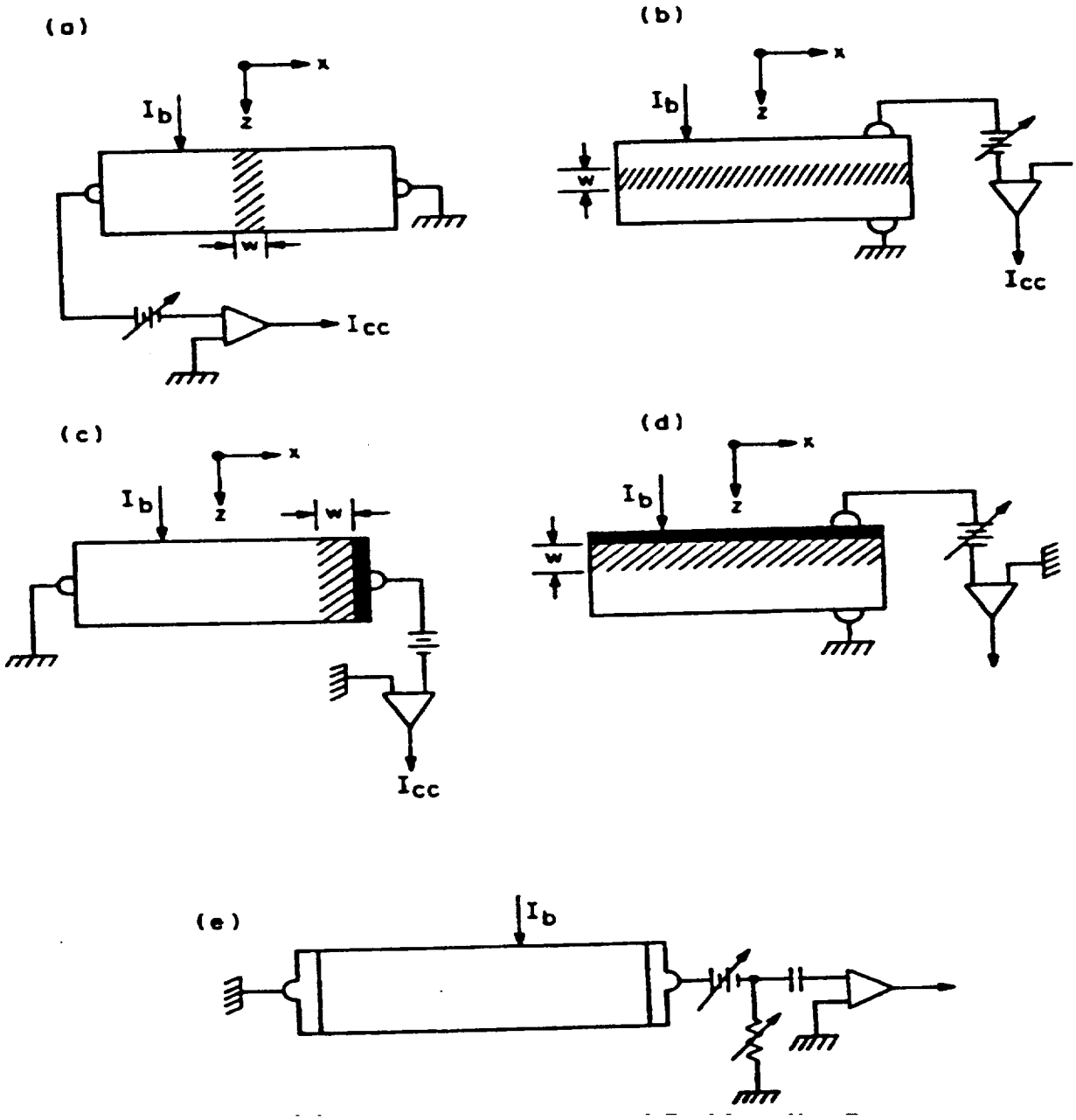

Figure 1.4 Illustration of the various EBIC setups. a) and b) show the linescan and planar methods for pn junctions. c) and d) show linescan and planar methods for Schottky barriers. Part e) shows the beta conductivity setup. (After Leamy, 1982).

decay with a decay constant equaling the diffusion length (Leamy, 1982). In a real device, where SRV is present, the equation for collected EBIC is more complex (Leamy, 1982; Donalato, 1982). These variations of EBIC are often referred to as linescan methods.

In Figures 1.4 b) and d), the incident electron beam is normal to the junction. In these cases, the collection efficiency of the diode is usually calculated from measured values of the collected current vs. depth of the generation volume. The beam penetration is adjusted by varying the energy of the incident electrons. By fitting experimental efficiencies with theoretical curves one may determine the diffusion length (Leamy, 1982; Wu and Wittry, 1978). These techniques are referred to as planar.

Figure 1.4 e) is an EBIC technique known as beta conductivity. In this technique, an external field is applied across the entire sample. In a fashion similar to the PC method, the change in conductivity is recorded due to a pulsed electron beam. This method will measure either lifetime or diffusion length. It has been discussed at length by Holt (1989).

A variation of the planar method is the planar linescan technique proposed by Ioannou and Dimitriadis (1982) and later modified to include surface recombination velocity by Chan, Ong, and Phang (1995). The setup for this technique is shown in Figure 1.5. In this technique, the Schottky contact (or thin n or p layer) covers only a portion of the sample. The decay of current is measured as the beam is scanned away from the Schottky contact. This decay can be used to determine the diffusion length (Ioannou and Dimitriadis, 1982). Appendix D describes some early work using this technique to measure minority carrier diffusion length in SiC.

The planar mapping technique, proposed in this thesis, makes use of a combination of both the planar technique and the planar linescan technique. In this technique, we scan our beam over the surface of the Schottky contact, measuring collected current at each point along the way. This scan is repeated for several different beam energies. These measured values of current are converted to efficiency as a function of beam energy for each position. The efficiency functions are fit to theory, and a diffusion length is extracted for each point along the linescan.

The EBIC techniques can also be used to produce images. An EBIC image is just a two dimensional linescan of the sample. Areas of higher collected current appear brighter, while areas where the EBIC current decreases appear darker. Figure 1.6 shows an EBIC image of defects in SiC. EBIC images are an excellent method for positional mapping of defects in a sample. An advantage of our planar mapping technique is that the diffusion length scan can be directly correlated to the corresponding EBIC image. In this way, visualization of the effect of defects on diffusion length is made possible.

In general, the linescan techniques are destructive measurements. The sample must be cleaved in order to expose the junction to the beam. In the planar and planar linescan techniques, we do not need to cleave the sample. A further benefit of the planar method is that the semiconductor surface is underneath the metal layer used to produce the Schottky barrier. In this case, surface recombination velocity will not effect the collected current. A summary of the techniques used to measure minority carrier properties is shown in Table 1.2.

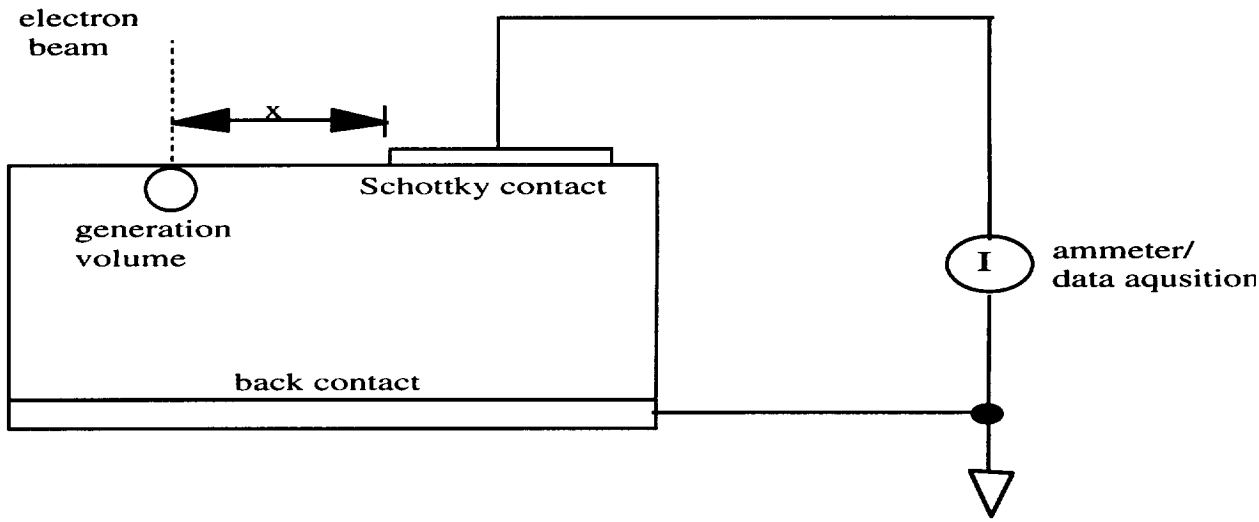

Figure 1.5 Representation of the planar linescan method.

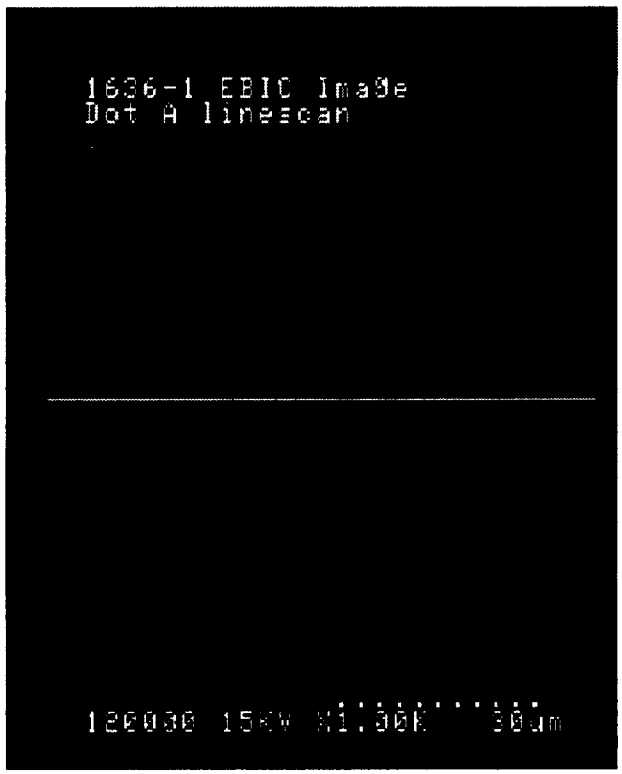

Figure 1.6 Typical EBIC image showing defects in 6H SiC.

Table 1.2 Methods used to measure minority carrier properties.

Method	Measures	Resolution Determined By	Type of Measurement	Contacts	Comments
Photoconductive Decay (PC)	τ	Pulsewidth of laser, electronics (amplifier, oscilloscope, etc.)	decaying photocurrent	Ohmic	Pulsewidth << τ
Photoelectromagnetic Effect (PEM)	τ	electronics	steady state current	Ohmic	Pulsewidth << τ
Photocurrent	L	electronics	steady state photocurrent	Rectifying	need optical properties of material
Haynes-Shockley	μ	Pulsewidth of laser; electronics	transient current	Ohmic	Difficult experimental setup
Storage Delay	τ	electronics	transient current	Rectifying	
EBIC					
-linescan	L	electron beamwidth; electronics	decaying EBIC	Rectifying	SRV problematic; beamwidth << L
-planer	L	electronics	steady state EBIC	Rectifying	need electron beam-solid interaction properties
-planer linescan	L	same as linescan	decaying EBIC	Rectifying	same as linescan
-planer mapping	L	electronics	steady state EBIC	Rectifying	same as planer
-β-conductivity	τ, L	electronics and beamwidth	transient EBIC	Ohmic	

Chapter II: Theory

2.1 Lifetime and Diffusion Length

As stated before, recombination lifetime is the mean time an EHP will exist before a recombination occurs. This recombination can occur as the result of a band to band transition, or can result from various trapping levels within the bandgap. Band to band transitions can result in emission of a photon in direct bandgap semiconductors, or emission of a phonon and a photon in indirect bandgap semiconductors. Trapping levels can be due to impurities introduced into the crystal (doping) or physical defects in the crystal lattice (dislocations). Figure 2.1 illustrates the different transition processes (Sze, 1991).

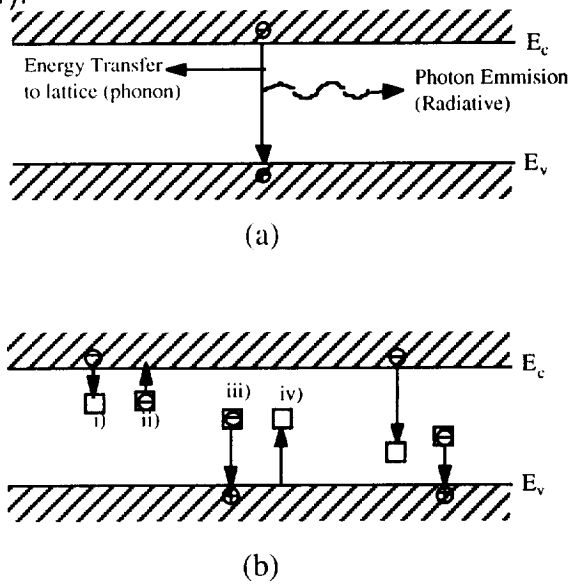

Figure 2.1 Recombination processes. a) Band to band recombinations, both direct and indirect. b) Multiple level trapping recombinations showing i) electron capture, ii) electron emission, iii) hole capture, and iv) hole emission.

By considering the recombination rate, it can be shown(Sze, 1981) that the lifetimes can be expressed as:

$$\tau_p = \frac{1}{\sigma_p v_{th} N_t} \qquad \text{(for holes in n-type material)} \qquad (2.1)$$

and

$$\tau_n = \frac{1}{\sigma_n v_{th} N_t} \qquad \text{(for electrons in p type material)} \qquad (2.2)$$

where σ_p and σ_n are the hole and electron capture cross sections, respectively, N_t is the trap density, and v_{th} is the thermal velocity given by:

$$v_{th} = \sqrt{\frac{3kT}{m^*}} \qquad (2.3)$$

where k is the Boltzmann constant, T the temperature in Kelvin, and m^* the effective mass.

As can be seen from Equations 2.1-2.2, recombination is dependent on the density of traps (N_t). It has been shown that impurities having energy levels near the middle of the bandgap are most effective in reducing the lifetime (Sze, 1981). For example, gold in Si, which has an energy level very near $E_g/2$, is often introduced in order to reduce the lifetime for switching applications. High energy irradiation, by causing interstitial defects, is another mechanism affecting the lifetime.

The mobility of a material describes how well a carrier type can move through the crystal lattice. Mobility is related to the carrier drift velocity, v_d, and electric field, E, by:

$$v_d = \mu E \qquad (2.4)$$

Generally, the mobility for electrons (μ_n) and holes (μ_p) are quite different.

The diffusion coefficient is another important parameter. We define the diffusion coefficients for electrons (D_n) and holes (D_p) from the classic Einstein relation for nondegenerate semiconductors:

$$\frac{D}{\mu} = \frac{kT}{q} \tag{2.5}$$

From Equation 2.4, we see that the mobility has units of $cm^2/V*s$, and from Equ. 2.5, the diffusion coefficient will have units of cm^2/s. Obviously, by combining the diffusion coefficient and the lifetime, we can produce a length that relates the diffusion of carriers to the recombination lifetime. We define this diffusion length as:

$$L \equiv \sqrt{D * \tau} \tag{2.6}$$

where the diffusion length of holes is L_p and electrons is L_n.

2.2 Metal-Semiconductor Junctions

Rectifying metal-semiconductor (M-S) junctions are referred to as Schottky barriers, after William Schottky, who first modeled barrier formation in M-S contacts. The potential barrier that forms when a metal contacts a semiconductor is due, as in a pn junction, to diffusion of charges, creating a region void of mobile charge carriers, referred to as the depletion zone. The effect of the metal layer is similar to an abrupt one sided pn junction (p^+n or n^+p), except in the case of a Schottky barrier, the potential barrier arises due to differences in the work function of the metal and that of the semiconductor.

The metal work function, ϕ_m, is defined as the energy required to move an electron from the metal's Fermi level to the vacuum level (see Figure 2.2). The semiconductor work function, ϕ_s, is similar, except that it will change as the semiconductor Fermi level varies due to doping. The electron affinity, χ_s, is defined as the difference in energy between the vacuum level and the conduction band edge. The electron affinity does not depend on doping and is usually the characteristic given in the literature.

Figure 2.2 a) & b) show the idealized band diagram for a titanium - 6H SiC n-type contact both before and after the contact is established. As can

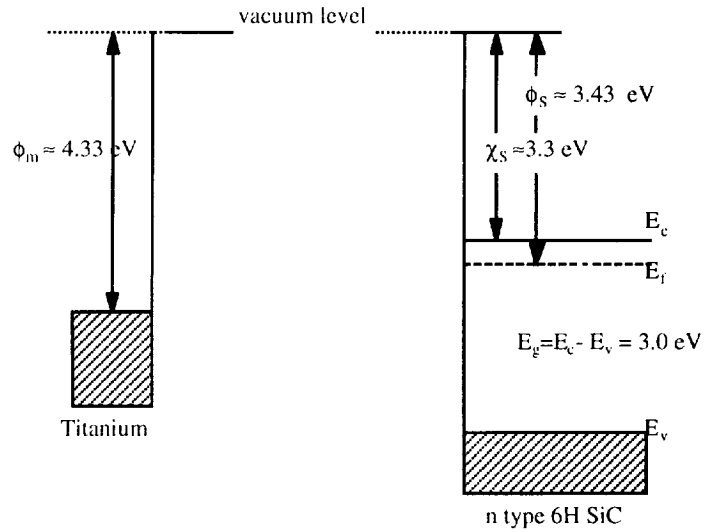

Figure 2.2a Band diagram of Titanium and 6H SiC before the metal semiconductor contact is made.

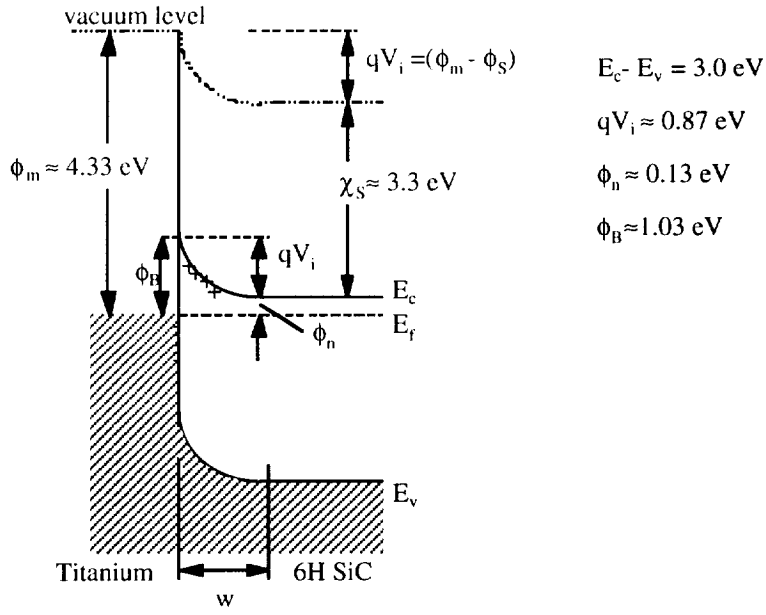

Figure 2.2b Band diagram after contact is made and equilibrium is established. Approximate values for barrier height and built in voltage are shown.

be seen from Figure 2.2 b), the barrier height for n-type material will depend on the semiconductor work function and electron affinity as:

$$\phi_B = (\phi_m - \chi_s) \tag{2.7}$$

Additionally, the semiconductor work function is given by:

$$\phi_s = (\phi_n + \chi_s) \tag{2.8}$$

In our example, Porter and Davis (1995) have given the electron affinity of 6H SiC as 3.3 eV. Very few measurements of affinity have been performed using SiC; therefore, for this work, we have used 3.3 eV.

The work function for titanium is given by Sharma (1984) as 4.33 eV. There is considerable variation in metal work functions given in the literature. Sharma's value is taken from Michalson (1978), who has attempted to theoretically account for the variation in reported metal work functions. Using these values, we calculate a theoretical barrier height for titanium-SiC of approximately 1.03 eV.

The difference between the Fermi level and the conduction band edge is shown as ϕ_n in Figure 2.2b. This value will depend on doping concentration. For n type 6H SiC with a donor concentration around 10^{17} cm^{-3}, we calculate the Fermi level to be nearly 130 meV below the conduction band (Sze, 1981). Thus, the semiconductors work function would be 3.43 eV and the built in potential 0.87 V.

The metal-semiconductor barrier is rectifying (Sharma, 1984), and has been modeled using a thermonic emission-diffusion theory (Sze, 1981). The IV characteristics of a Schottky diode are given as:

$$J = J_0[\exp(\frac{qV}{\eta kT}) - 1] \tag{2.9}$$

where J is the current density, J_0 the reverse saturation current density, and V the voltage. We refer to η an the diode ideality factor. Its value is close to one for low doping and higher temperatures. At higher doping and decreased temperature the ideality factor can vary substantially from unity.

Additionally, diode nonideality can affect the ideality factor. Interfacial states and recombinations within the depletion region will increase the value of ideality. A non-unit value of ideality indicates the combined effects of interfacial states, space charge recombinations, doping and temperature.

If we rearrange Equation 2.9 and take the natural logarithm, we find that:

$$\ln(J) = \frac{q}{\eta kT} V - \ln(J_0) \tag{2.10}$$

where we assume that V is greater than a few kt/q's, so that the factor of one can be ignored. This equation is linear in voltage, where the slope is related to ideality factor and the y-intercept is the log of saturation current density. Experimental values of J verses V can be fit to Equation 2.10 using a simple linear regression technique. From the slope and intercept of the linear regression we can determine the experimental diode ideality factor and saturation current density.

Additionally, the saturation current can be related to the barrier height by (Sze, 1981):

$$J_s = A^* T^2 \exp(-\frac{q\phi_B}{kT}) \tag{2.11}$$

where A^* is the modified Richardson constant. The modified Richardson constant can be approximated using the following (Sze, 1981):

$$A^* = \frac{4\pi q m^* k^2}{h^3} \tag{2.12}$$

where m^* is the effective mass of electrons. In alpha SiC, the approximate effective mass is given (Sze, 1981) as $0.6m_0$. The modified Richardson constant for SiC was found to be:

$$A^* = 72 \frac{A}{cm^2 K^2} \tag{2.13}$$

Therefore, using our experimental values of J_s and Equation 2.11, we can calculate values of barrier height for our Schottky diodes.

The depletion width of a Schottky diode, w in Figure 2.2, is similar to an abrupt one sided p^+n junction. It is given as:

$$w = \sqrt{\frac{2\varepsilon_{SiC}}{qN_D}(V_i - V - \frac{kT}{q})} \tag{2.14}$$

where ε_{SiC} is the permativity of SiC, which is given as 10 ε_0 (Sze, 1981), and N_D is the donor density.

If we consider the capacitance created by the depletion region, we find:

$$C = \frac{\varepsilon_{SiC} A}{w} = A \sqrt{\frac{q\varepsilon_{SiC} N_D}{2(V_i - V - \frac{kT}{q})}} \qquad (2.15)$$

where A is the diode cross sectional area. By rearranging the capacitance equation to be linear in voltage, we arrive at:

$$\frac{1}{C^2} = \frac{2(V_i - V - \frac{kT}{q})}{A^2 q \varepsilon_{SiC} N_D} \qquad (2.16)$$

From Equation 2.16 we see that from the slope of $1/C^2$ we can find the doping concentration of the material:

$$N_D = \frac{-2}{(\frac{\partial(1/C^2)}{\partial V} A^2 q \varepsilon_{SiC})} \qquad (2.17)$$

Therefore, using experimental values of capacitance versus voltage and linear regression, we can determine the doping concentration of our material. Additionally, from Equation 2.16 we see that from the intercept of $1/C^2$ we can calculate the built in voltage.

2.3 The Planar EBIC Techniques

2.3.1 Electron Beam-Solid Interactions

Over the past 25 years, the Scanning Electron Microscope (SEM) has developed into a powerful tool for the characterization of semiconductors. The operating principle of the SEM is fairly simple. A high energy electron beam is used to bombard a sample's surface. The electrons interact with the solid, producing some type of resultant radiation (photon, electrons, x-rays,

etc.). The secondary effects of the electron solid interaction are detected using an appropriate detector. The output of the detector can then be used to form an image. Further reading on electron optics and SEM theory can be found in Holt and Joy (1989) or Goldstein *et al.* (1984).

As mentioned above, secondary radiation resulting from electron bombardment can take various forms. In all cases, it is electron scattering within the crystal that causes this radiation. Scattering can take two forms, either elastic or inelastic. In elastic scattering, the electrons trajectory will change, but its energy will remain essentially unchanged. Inelastic scattering occurs when the electron imparts some of its energy to the solid. Inelastic scattering can result in the production of secondary electrons, backscattered electrons, Auger electrons, characteristic and continuum x-rays, long-wavelength radiation in the visible, ultraviolet and infrared regions, electron-hole pairs, lattice vibrations (phonons), and electron oscillations (plasmons).

The effect most often used for imaging is secondary electron emission. In this process, the incident beam electrons impart enough energy to the solid's electrons to eject them beyond the vacuum level of the atom. A secondary electron must then escape the sample's vacuum level in order to be detected. Those electrons created deeper within the sample usually undergo further scattering events, decreasing the probability of that electron having enough energy to surmount the samples work function. Therefore, the majority of secondary electrons come from very near the samples surface. Secondary electron imaging is an excellent tool for measuring surface morphology of a sample.

Of critical importance to our studies is the effect of electron-hole pair generation. Essentially, the generated electrons in EHP formation are those electrons that did not escape the sample in the secondary electron process. Instead of "knocking" the electron out of the sample, the incident beam has only succeeded in transferring electrons to the conduction band.

The final effect that needs to be addressed in this study is backscattered electrons. Backscattered electrons are those incident beam electrons whose trajectory intersects the samples surface. These electrons are scattered back into the surrounding environment. It has been shown that as much as 30% of incident beam electrons are backscattered (Goldstein *et al.*, 1984).

The actual shape and maximum penetration range of the electron trajectories is also of interest. There are three main ways to determine this information: experimentally, computer simulation, or theoretical modeling. Experimental measurements are done using penetration of electrons through a thin film. This method must be performed on a thin film and can provide range data, but not the shape of the interaction volume. Computer simulation is done using Monte Carlo techniques. Monte Carlo simulation is

a particularly useful tool in electron-solid interaction studies and can provide both range and shape information for any material as long as the atomic number is known. Monte Carlo simulations were not performed during our studies. All of our range data was calculated theoretically, as described below.

2.3.2 Wu and Wittry's Method

The following theory is based on the work of Wu and Wittry (1978), who have derived theoretical expressions for Electron Beam Induced Current(EBIC) using the standard continuity and current density relations. In this technique, high energy electrons are used to irradiate the sample, causing a generation volume of EHP's, as shown in Figure 2.3. These generated carriers diffuse toward the junction, where they are collected and

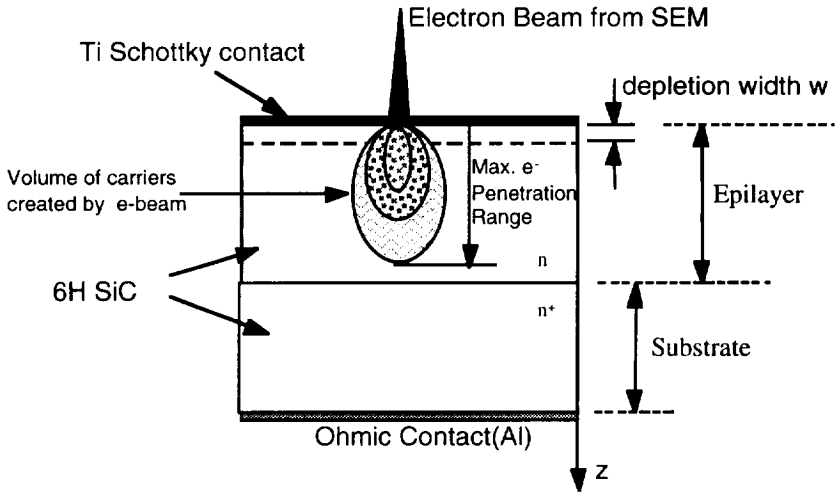

Figure 2.3 Setup for EBIC measurement in 6H SiC.

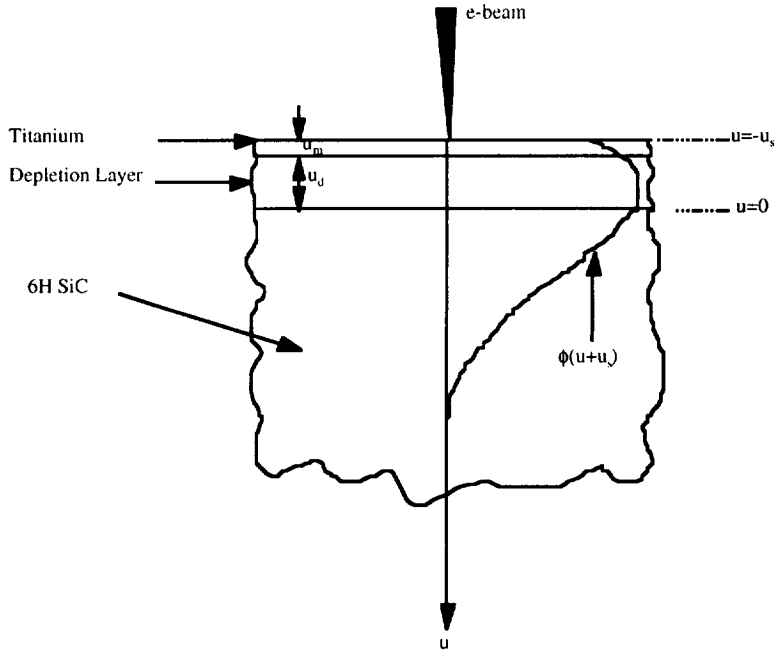

Figure 2.4 Setup of experiment using the dimensionless coordinate u. (After Wu and Wittry, 1978).

measured as the EBIC. The diffusion length of the material will dictate the number of carriers that will diffuse to the junction and the number that recombine before that point.

In this theory, a modified Gaussian distribution has been used to model the electron distribution within the sample. This distribution is given by Kyser (1971) as:

$$\phi(u) = A\exp[-(\frac{u-u_0}{\Delta u})^2] - B\exp(-\frac{bu}{u_0}) \qquad (2.18)$$

where $u=\rho z/R$, ρ is the density of SiC, z is the depth as seen in Figure 2.3, and R is the density normalized maximum penetration range in g/cm^2. The constants for the Gaussian distribution calculated by Kyser using Monte Carlo are: $u_0=0.125$, $\Delta u=0.350$, $b=4$, and $B/A=0.4$. These constants are given for GaAs, and will change very slightly with atomic number. Wu and Wittry (1978) have successfully applied these constants to both GaAs and Si. As SiC is similar in atomic number to Si, we have also used these constants. Exact values of these constants for SiC could be determined in future work using Monte Carlo techniques.

In order to simplify calculations, the dimensionless variable u has been introduced as a coordinate with origin at the semiconductor-depletion layer boundary. Figure 2.4 shows the setup in the new coordinate system. Using the above generation function, we consider the one dimensional steady state continuity equation, expressed in the dimensionless coordinate system as:

$$\frac{d^2\Delta p}{du^2} - w^2\Delta p + (\frac{wL}{D_p})\phi(u+u_s) = 0 \qquad (2.19)$$

where $\Delta p(u)$ is the excess carrier density, D_p the diffusion coefficient, and L the diffusion length. Additionally we define $w=R/\rho L$ to be the reduced electron range; $u_s=u_m+u_d$, with $u_m=\rho_m z_m/R$ being the reduced metal thickness, where ρ_m is the metal density and z_m is the metal thickness, and $u_m=\rho_{SiC} z_d/R$ is the reduced depletion layer width with z_d being the depletion layer thickness.

In order to arrive at the boundary conditions we make three key assumptions. In the metal region, we assume all energy is dissipated without generation of EHP. In the depletion region, we assume all carriers generated are collected. This means that there should be few

recombinations or trapping processes in the depletion region. Finally it is assumed that those carrier in the bulk that make it to the depletion zone boundary are collected with unit efficiency. Based on these assumptions we state the boundary conditions as:

$$\Delta p(u=0)=0 \tag{2.20}$$

$$\Delta p(u=\infty)=0 \tag{2.21}$$

Wu and Wittry solve this equation by first replacing the generation function by a delta function $\delta(u-u')$ located at position u'. This produced a second order nonhomogeneous differential equation, which was solved using Laplace transforms. The given solution is:

$$\Delta p(u)=(\frac{L}{2D_p})\{\exp[-|u-u'|w]-\exp[-(u+u')w]\} \tag{2.22}$$

Which is then applied to the original generation function using:

$$\Delta p(u)=(\frac{L}{2D_p})\int_0^{\infty}\{\exp[-|u-u'|w]-\exp[-(u+u')w]\}\phi(u'+u_s)du' \tag{2.23}$$

The solution of this integration is then applied to the current density equation in order to find the current density in the bulk. The final solution is:

$$J_b=-qD_p(wL)^{-1}\left.\frac{d\Delta p}{du}\right|_{u=0}$$

$$=-qA(\frac{\sqrt{\pi}\Delta u}{2})\exp[\alpha w+(\frac{w\Delta u}{2})^2]erfc(\frac{\alpha}{\Delta u}+\frac{w\Delta u}{2})$$

$$+\frac{qB}{\frac{b}{u_0}+w}\exp(-b\frac{u_s}{u_o}) \tag{2.23}$$

where erfc(x)=1-erf (x) and $\alpha=u_s-u_o$. The constants A and B are determined by requiring that the integral of the generation function over the entire sample be equal to the total carrier generation due the incident beam. This normalization condition is given as:

$$\int_{-u_s}^{\infty} \phi(u+u_s) = G_0 \tag{2.24}$$

using the previous relation B/A=0.4 we calculate the constant A to be:

$$A = \frac{G_o}{\frac{1}{2}\sqrt{\pi}\Delta u[1+erf(\frac{u_o}{\Delta u})] - 0.4(\frac{u_o}{b})} \tag{2.25}$$

The total carrier generation rate is given as:

$$G_o(cm^{-2}\sec^{-1}) = 1000\frac{V_o j_{beam}}{q\varepsilon}(1-\eta\frac{\overline{V}}{V_o}) \tag{2.26}$$

where V_0 is the incident electron beam voltage in kV, j_{beam} is the incident beam current density, η is the fraction of incident electrons backscattered, $\overline{V}$ is the mean energy of backscattered electrons in kV, and ε is the mean energy required to generate a electron-hole pair in eV.

The collected current in the depletion region, because we assume unit collection efficiency, is due only to the generation function. Thus:

$$\begin{aligned} J_d &= -q\int_{-u_d}^{0} \phi(u+u_s)du \\ &= -qA(\frac{\sqrt{\pi}\Delta u}{2})[erf(\frac{\alpha}{\Delta u}) - erf(\frac{u_m-u_o}{\Delta u})] \\ &+qB(\frac{u_o}{b})[\exp(-b\frac{u_m}{u_o}) - \exp(-b\frac{u_s}{u_o})] \end{aligned} \tag{2.27}$$

Therefore, the total collected current density is given by:

$$J = J_b + J_d \tag{2.28}$$

The total current available for collection is just qG_o so that the collection efficiency is just:

$$e = \frac{|J|}{qG_o} \tag{2.29}$$

The collection efficiency is a function of the collected current and the total generation rate; but, the constants A and B contained in J are themselves functions of G_o, so that the collection efficiency is actually only a function of theoretical collected current, which will depend on the following four variables:

$$e = f(R(V_o), L, z_m, w) \tag{2.30}$$

As can be seen above, a knowledge of maximum penetration range versus beam voltage is required. This range has been derived from both experiment and theory. The experimentally derived range is given by Gruen (1956). Theoretically derived expressions are given by Everhart & Hoff (1971), Kanaya & Okayama (1972), and Wittry & Keyser (1967). We have used the Wittry-Kyser range relation in our calculations. This relation, normalized for density, is given as:

$$R(V_o) = 2.56 * 10^{-3} (\frac{V_o}{30})^{1.7} g/cm^2 \tag{2.31}$$

Using Equation 2.29 and knowledge of $R(V_o)$ we can calculate theoretical collection efficiency curves for our setup. These curves are shown in Figure 2.5. Here we have held the depletion width and metal layer thickness constant, and varied the diffusion length. As can be seen in Figure 2.5, the efficiency curves are sensitive indicators of changes in diffusion length. Therefore, by comparing experimental efficiency to theoretical efficiency, we can extract diffusion length.

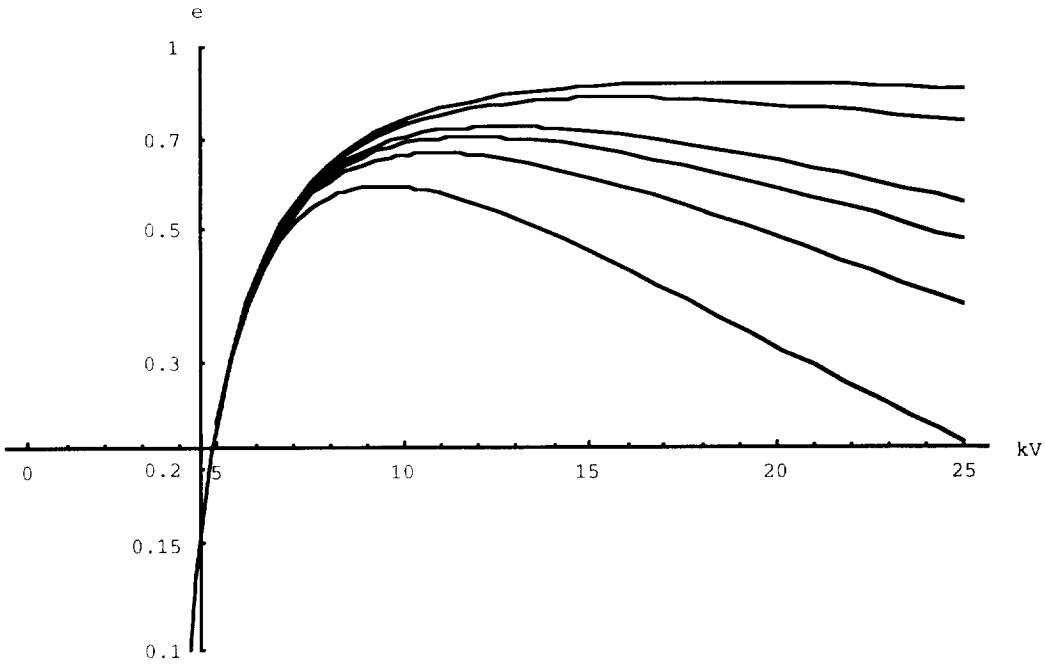

Figure 2.5 Theoretical EBIC collection efficiency e for Ti on 6H SiC Schottky barrier diodes. We assume that z_m=1000Å and z_d=1000Å with various diffusion lengths.

Chapter III: Experimental Procedure

3.1 Sample Preparation

3.1.1 Sample Growth

Four 6H SiC samples have been studied in this work. These shall be referred to as Sample A, Sample B, Sample C, and Sample D. In all cases, the substrates were 6H SiC grown by Cree Research. The epilayers for Samples A, B, and C were grown at NASA Lewis Research Center in Cleveland, OH. Sample D was a photodiode produced commercially by Cree Research.

The substrates for Samples A, B, and C were n^+ 6H SiC wafers of approximately 25.4 mm in diameter. These substrates were grown using the modified Lely seeded sublimation technique. The wafers were sliced approx. 200 μm thick and polished 3^o to 4^0 off the (0001) axis toward the $[11\bar{2}0]$ direction. This type of substrate is often referred to as vicinal (0001) SiC. The layer of atoms at the surface interface was Si for all of our samples.

The common method of indicating planes in hexagonal crystals uses a modified Miller index (Sze, 1981). This index is given by $[a_1a_2a_3c]$, where the directions are as given in Figure 3.1. The basal plane is given as [0001]. A bar above the index indicates the negative of that vector.

The epilayers for Sample A-C were produced by P. Neudeck at NASA Lewis Research Center. Before growth, the wafers were cut into smaller sample sizes (Table 3.1). Epilayers were grown n-type using Larkin's site-competition CVD. The growth process is described in detail by Powell *et al.* (1990) and Larkin *et al.* (1994). Table 3.1 lists the growth parameters for Samples A-C.

Sample C had Pd Schottky contacts made by Gary Hunter at NASA Lewis Research Center. Details of the contact procedure can be found in Hunter *et al.* (1995).

Sample D was a commercially produced Cree photodiode. Its basic structure is shown in Figure 3.2. The junction was thin n^+ on p, therefore we can consider it to be similar to a Schottky barrier, allowing us to use Wu and Wittry's planar EBIC technique to extract diffusion length. A detailed explanation of this type of photodiode is given by Brown *et al.* (1993).

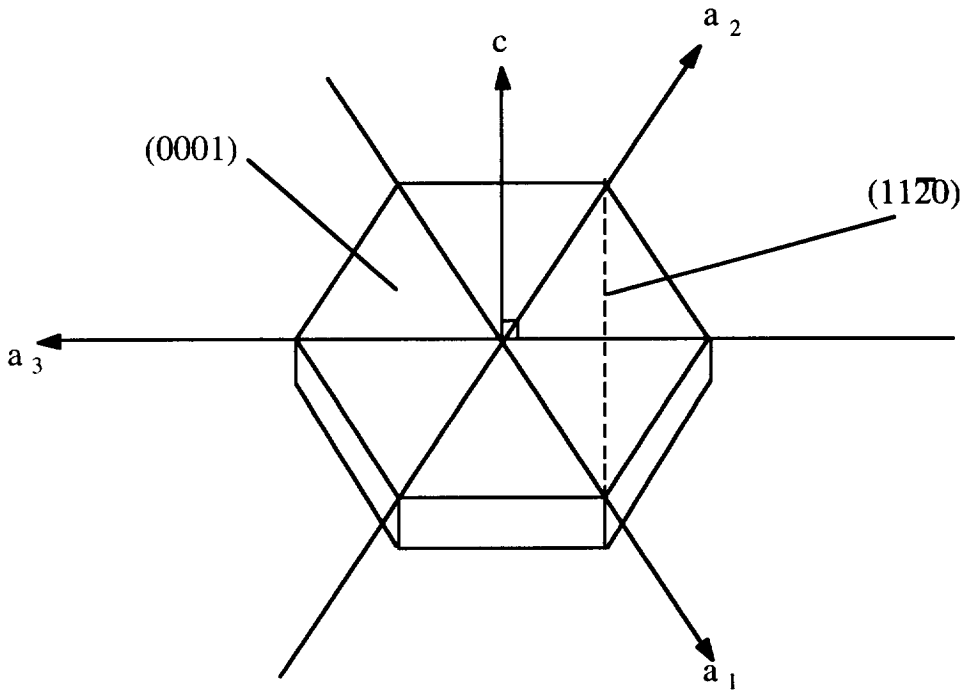

Figure 3.1 Index system used with hexagonal crystal structure.

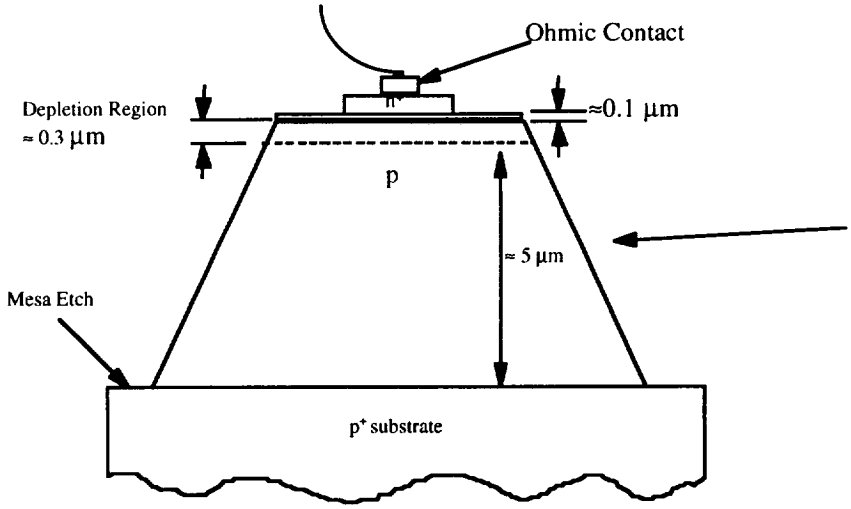

Figure 3.2 Structure of Sample D, a Cree Research UV photodiode.

Table 3.1 Growth history for samples used in this study.

Sample	Type	Dopant	Substrate Growth and Orientation	Epilayer Growth	Epilayer Thickness	Top Face	Sample Size	Reference
A	n/n^+	N	Cree, vicinal (0001)	NASA, CVD	4-6 μm	Si	6mm X 7mm	Larkin, 1990 Larkin, 1994
B	n/n^+	N	Cree, vicinal (0001)	NASA, CVD	10 μm	Si	6mm X 7mm	Larkin, 1990 Larkin, 1994
C	n/n^+	N	Cree, vicinal (0001)	NASA, CVD	4-5 μm	N/R	3 mm x 3mm	Hunter, 1995
D	$n^+/p/p^+$	N/Al	Cree, not reported(N/R)	Cree, CVD	≈5 μm	N/R	1 mm x 1mm	Brown, 1993

3.1.2 Preparation for Deposition

Samples A and B were cleaned using the following procedure:

1.) Sample A was etched in hot (80° C) HCl for 10 min., then room temperature NaOH for 10 min., in order to remove an old AlO_2 film from the surface.

2.) Both Sample A and Sample B were acid cleaned in HCl for 3 min., then dipped in conc. HF. This procedure ensured a clean sample surface.

3.) After the acid cleaning, samples were cleaned in acetone, then propanol, rinsed in DI water, and finally blown dry with compressed nitrogen.

Samples A and B were then stored in Teflon containers awaiting metal deposition.

3.1.3 Deposition Techniques

Titanium contacts were formed on Samples A and B using thermal evaporation of Ti, then photolithography, then etch. A blanket evaporation of Ti was performed using an MRC V-4 Series diffusion pumped thermal evaporator. The film thickness was monitored using an Sycon Instruments STM-100 Quartz Crystal Thickness Monitor. The monitor calibration is documented in Appendix A.

Immediately prior to deposition, the samples were "quick dipped" in a buffered HF solution in order to remove surface oxides. After the HF dip, the samples were quenched in DI water, then blown dry with compressed nitrogen.

The samples were mounted in the evaporator approximately 25 cm above the thermal boat source. The thermal boat source was then filled with 99% pure Ti pieces. The evaporator was closed, flooded with nitrogen gas, then pumped down to $8.5*10^{-7}$ Torr using a combination of the diffusion pump and a liquid nitrogen "cold trap". The boat source was slowly heated until the Ti pieces melted. At this point, a shutter was opened, exposing the samples to the source. We then evaporated 1500Å of Ti, monitoring the thickness using the quartz thickness monitor. The evaporator was allowed to cool for 20 minutes before the samples were removed.

3.1.4 Diode Formation

The Schottky diodes were formed using photolithography and etching. A 3 μm reverse photoresist (Hoechst Celarese AZ1529) was spin coated on both Sample A and B using a Headway Research, Inc. Model EC101 spin

coating unit. The samples were allowed to cure at room temperature for approx. 2 hours. At this point, the samples were covered with a positive photomask and irradiated with UV for 30 seconds using an HTG 84-2 Lightsource. The samples were then baked at 97° C for 35 minutes.

After the bake, the samples were blanket exposed to UV radiation for an additional 30 seconds, then developed using a 4:1 mixture of DI water to developer. The developer was Hoechst Celarese AZ351 Developer, containing sodium borates and water. The samples were allowed to remain in the developer until a clear pattern was visible (approx. 30 seconds), then were quenched in DI water for 1 minute and blown dry with nitrogen. Finally, a "hard bake" at 130° C for 20 minutes was performed.

The result of the above photolithography processing was that a negative mask design was created on the samples. The photoresist still covered the sample in spots where the contacts were to be formed, but was removed from all other areas. By etching the samples in a dilute (60:1) HF solution for 20 seconds, excess titanium around the contacts was removed. The photoresist still covering the contacts was removed with acetone in an ultrasonic bath. Images of the resulting diode pattern can be seen in Chapter 4.

3.1.5 Ohmic Contacts

Ohmic contacts were made to the back (n^+) unpolished side of Sample A and B using Al. This was done using the MRC thermal evaporator in the same manner as Section 3.1.3, except 99.999% pure Al was loaded into the source before evacuation. Using the quartz thickness monitor, we deposited 3000Å of Al as an ohmic contact. The entire backside of the sample was covered, patterning of the contact was not performed. The results of all of the above processing is shown in Table 3.2. Additionally, contact information given in the references for Sample C and D is shown.

Table 3.2 Contact Information for the samples used in this study.

Sample	Junction Type	Schottky contact	Schottky Thickness	Ohmic contact	Ohmic thickness
A	Schottky	Ti	1500Å	Al	3000Å
B	Schottky	Ti	1500Å	Al	3000Å
C	Schottky	Pd	300-400Å	Al	N/R
D	thin n^+ on p	n^+ 6H SiC epilayer	≤1000Å	Au on n^+, p^+ not reported	N/R

3.2 Characterization of the Test Devices

3.2.1 Measurement of IV Characteristics

Current versus voltage characteristics for our diodes were measured using a Keithley 238 High Current Source Measure Unit. This instrument was controlled by a PC interfaced through an IEEE 488 interface and driver software. The 238 was connected to the device under test (DUT) using microprobes and a vacuum table.

A computer program in Turbo C was used to control the 238. This program allowed the user to select the start and stop point of the voltage scan, bias level, and number of data points to be taken. The data points (voltage, current) were stored in an ASCII text file.

This text file was then imported into a Microsoft Excel 5.0 worksheet. A linear regression of the data was done using the standard Microsoft Excel linear regress function. From the regression data, we calculated values of ideality factor, saturation current, and barrier height as shown in Chapter 2.

3.2.2 Measurement of CV Characteristics

Capacitance versus voltage measurements were taken using a Keithley 590 CV Analyzer. This unit was also interfaced to a PC using an IEEE 488 bus and driver software. The DUT was places on the same vacuum table and probed with the same microprobes as Section 3.2.1.

A Quick Basic 4.0 program was used to control the 590. This program allows the user to input the maximum bias and the output file name. The program then records the capacitance versus voltage data, and additionally calculates $1/C^2$. The data (voltage, capacitance, $1/C^2$) is stored in an ASCII text file.

This text file was then imported into a Microsoft Excel 5.0 worksheet. As in Section 3.2.1, linear regression of the data was done using the standard Microsoft Excel linear regress function. From the regression data, we calculated the doping concentration using the equations shown in Chapter 2.

3.3 Planar EBIC Technique

3.3.1 Measurement of EBIC and Beam Current

A Hitachi S-800 Field Emission Scanning Electron Microscope was used to bombard the sample with electrons. Figure 3.3 shows a schematic of the experimental setup. The S-800 had an adjustable beam voltage from 1-25 kV in 1kV steps. Measurements of collected EBIC versus beam voltage were made at room temperature and a moderate Sample Container vacuum ($\approx 10^{-6}$ Torr).

The EBIC measurements were made possible through the use of a special EBIC sample stub which allowed the sample to be connected through a coaxial feedthrough in the SEM Specimen Chamber wall to a GW Electronics Type 31 Specimen Current Amplifier. Figure 3.4 is a photograph of the EBIC sample stub.

As can be seen from Figure 3.4, the EBIC stub has two electrically isolated sections. The main body of the stub fit into the SEM sample stage, which was grounded. The backside of the sample was connected to the main body of the stub using silver paint. The clip was attached to the Schottky contact. A spring clip on the sample stage contacted the metal ring on the EBIC stub. The spring clip was attached to a coaxial cable which was then attached to the coaxial feedthrough in the wall of the SC.

EBIC was measured as a function of beam voltage, typically 22 EBIC points were recorded, from 4kV to 25kV in 1kV steps. EBIC below 4kV was too small to be measured using the GW Specimen Current meter. The electron beam diameter was kept between 1-2 μm. This large beam diameter was used to ensure low injection levels during EBIC measurements.

Additionally, beam current was recorded using a Faraday cup mounted on the EBIC stub. The Faraday cup is a completely closed container except for a small entrance aperture. The Faraday cup will not allow the secondary or backscattered electrons to escape. Therefore, the current to ground will be equal to the incident beam current.

The aperture was a 1mm hole drilled into a thin brass plate (see Figure 3.4). A larger diameter hole (2mm) was drilled underneath the plate. The beam could be positioned over the hole and beam current recorded using the GW Type 31 meter. Beam currents ranged between $5*10^{-9}$ Amperes for higher beam voltage to $5*10^{-11}$ Amperes for low beam voltage.

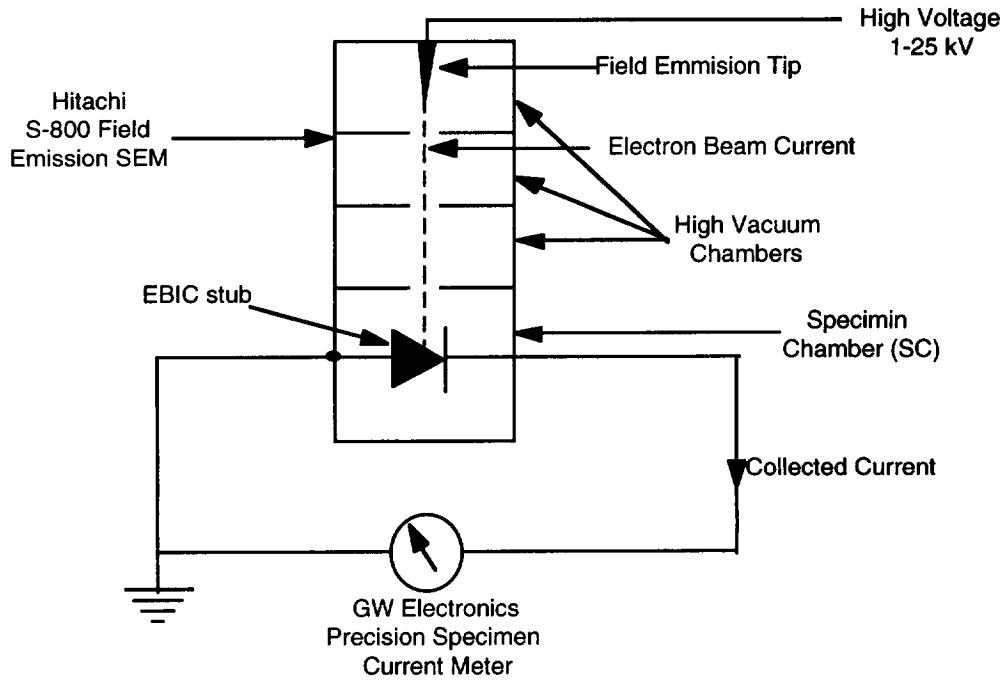

Figure 3.3 Schematic of the experimental setup.

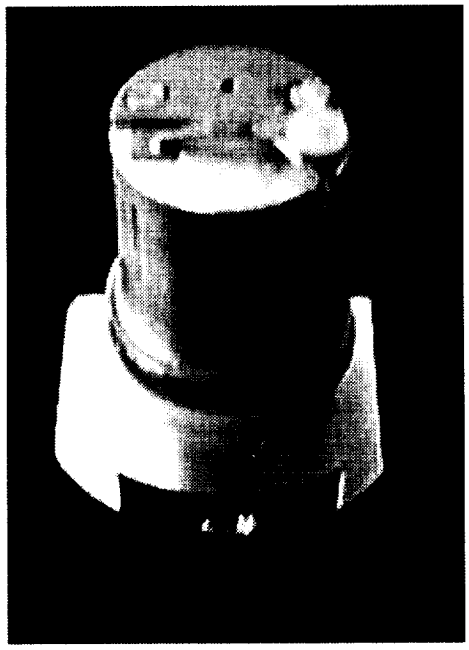

Figure 3.4 Photograph of the EBIC sample stub.

3.3.2 Calculation of experimental collection efficiency

Experimental collection efficiency was calculated using the following equation:

$$e = \frac{|J|}{qG_o} = \frac{\varepsilon I}{1000 V_o i_{beam} (1 - \eta \frac{\overline{V}}{V_o})} \qquad (3.1)$$

where I was the EBIC and i_{beam} was incident electron beam current measured with the Faraday cup.

The value of the electron-hole pair generation energy, ε , has been shown to be linearly related to the bandgap of the material (Klein, 1968). An empirical relation based on a fit to experimental data has been given by Ehrenberg and Gibbons(1981):

$$\varepsilon = 2.1 E_g + 1.3 \qquad (3.2)$$

where E_g is the bandgap of the material. For 6H SiC, with a bandgap of 3 eV, we found the EHP formation energy to be 7.6 eV.

The value of η indicates the fraction of incident electrons that are backscattered. This backscatter fraction has been shown to increase with atomic number (Goldstein *et al.*, 1984). Additionally, the backscatter fraction has been shown to decrease very slightly with increased beam voltage for low atomic numbers, and to increase with increased beam voltage for larger atomic numbers. The above assertions have been shown experimentally by Heinrich (1966).

For SiC, whose average atomic number is 10, the backscatter fraction will change very little with beam voltage. We have used Reuter's (1972) fit to Heinrich's 20 keV data, and allowed η to remain constant throughout our calculations. The fit is given as a function of atomic number Z:

$$\eta = -0.0254 + 0.016Z - 1.86 * 10^{-4} Z^2 + 8.3 * 10^{-7} Z^3 \qquad (3.3)$$

Additionally, for compound materials, a simple mixture relation based on weight fraction is found to apply (Heinrich, 1966):

$$\eta_{SiC} = 0.7\eta_{Si} + 0.3\eta_C \qquad (3.4)$$

Therefore, using Equations 3.3 and 3.4, we found the backscatter fraction for SiC to be 0.134. A review of Heinrich and Reuter's work is found in Goldstein *et al.* (1984).

The value of $\overline{V}$ describes the mean energy of backscattered electrons. An approximation to this value has been proposed by Sternglass (1954) and is given as:

$$\overline{V} = (0.45 + 2 * 10^{-3} Z)V_o \qquad (3.5)$$

The mean backscatter energy is further multiplied by η, which is a small fraction (13%), so that e is weakly dependent on the value of $\overline{V}$. The above approximation to the real mean backscatter energy was adequate for our efficiency calculations. In the case of SiC, the mean backscatter energy using Equation 3.5 was found to be $0.47V_0$.

Our calculated backscattered correction factor, $(1-\eta\frac{\overline{V}}{V_o})$, for SiC was found to be 0.93. Experimentally, the backscatter correction factor for Si has been shown to be consistently near 0.9 for a number of different beam voltages between 1 kV and 60 kV (Bishop, 1966). As SiC is very close in atomic number to Si, a constant value of 0.93 should be a reasonable value of backscatter correction efficiency.

3.3.3 Extraction of Diffusion Length

Values of EBIC versus beam voltage were recorded manually in a log book. Additionally, beam current data was recorded in the log book both before and after the measurement of the EBIC values. By taking beam data both before and after EBIC measurement, error in calculated efficiency due to drift in beam current could be determined. If a discrepancy in beam current data before and after was discovered, the higher value was used. Recorded values of EBIC and beam current were entered into a Microsoft Excel 5.0 spreadsheet and saved as an ASCII text file.

A program in Mathematica 3.0 was written in order to calculate the experimental efficiency and extract the diffusion length. Appendix B gives a listing of the program. This program first reads in the raw data from the text file and calculates the experimental efficiency. Using the nonlinear fit routine in Mathematica, the experimental efficiency was fit to theoretical efficiency and a diffusion length extracted. This nonlinear fit is based on the

Levenberg-Marquardt Method described in the book "Numerical Recipes" by W.H. Press *et al.* (1989).

The range energy relation was calculated using Equation 2.31, and the depletion width was calculated using Equation 2.14. Diffusion length and metal layer thickness were used as fit parameters. Starting points for diffuison length and metal layer thickness were based on previously reported values of L in SiC (Anakin, 1992) and thickness monitor readings, respectively. The goodness of the fit was qualitatively verified by plotting the experimental collection efficiency on top of theoretical efficiency using the parameters given by the nonlinear fit. These plots are shown in Appendix C.

In addition, secondary electron (SE) and EBIC images were recorded for each extracted diffusion length. These images were recorded electronically in JPEG format. This was accomplished using a PC interface and GW Electronics' Printerface for Windows 2.0 software.

3.4 The Planar Mapping Technique

In the planar mapping technique, we combine the linescan with the planar method. In the planar method only EBIC(V) was recorded. In the planar mapping technique we now record the two dimensional quantity EBIC(V,x). This 2-D measurement was accomplished using a computer controlled interface to the SEM and a Mathematica 3.0 program.

The S-800 was controlled using an Hitachi EMO-2790 interface bus, a MetraByte DAS-16 data acquisition card, Asyst 3.01 software, and a PC. The software and interface were designed by Carroll Robinson of the Kent State University School of Technology.

The Asyst program allowed the user to enter number of data points to be taken, the total scan time, the range of the GW Type 31 meter, length of the scan (from 10%-100%), number of points per position (average value for each position is calculated), and position of scan. All of our scans used the following parameters: 100 data points, 20 second scan time, various ranges depending on actual values of current, 80% line scan, 10 points per position, and various positions indicated by the white line in the EBIC images in Chapter 4. When the program was run, the PC took control of the electron beam and scanned it across the sample using the parameters given above. Data was stored as measured current versus beam position, given as a number between 1 and the total number of points (100 in all our studies). One scan was performed for each voltage, from 5 to 25 kV. The Asyst program stored the current versus beam position data for each scan as a separate ASCII text file. As before, beam current data was recorded both before and after the EBIC scans.

The Mathematica 3.0 program used for the planar mapping technique is shown in Appendix B. This program will read in all of the EBIC text files and calculate a EBIC matrix, with the column position indicating scan voltage and row position indicating beam position. Additionally, beam current data is read in from an ASCII text file, and a collection efficiency matrix is calculated from the EBIC matrix and beam current data. Each row of the collection efficiency matrix is fit using the nonlinear fit routine in Mathematica. The resulting diffusion length versus beam position data is plotted to the screen, and then stored in a ASCII text file.

A visualization of the effect of the defects on diffusion length was accomplished by overlaying the plot of diffusion length on top off the corresponding EBIC image. This was done using the features of Adobe Photoshop 3.0. The results can be seen in Chapter 4.

Chapter IV: Results and Discussion

4.1 Planar EBIC Results

The planar method was used to map diffusion length over the surface of Sample A. A diffusion length was measured for defect free areas of various Schottky contacts. The map of the contacts studied is shown in Figure 4.1.

For each contact we performed an IV analysis and calculated the ideality factor, Saturation Current Density, and Barrier Height. These values were calculated using the theory and methods shown in Chapters 2 and 3. Plots of the natural logarithm of current density versus voltage are shown in Figure 4.2. The results of our IV analysis are shown in Table 4.1.

Diode ideality factors ranged from 1.12 to 1.21. This indicates slight diode nonideality. We would expect these diodes to have little space charge recombination and a low density of surface states. Saturation current densities ranged from approx. 0.6 mA/cm^2 to 0.02 mA/cm^2. These current densities resulted in barrier heights ranging from 0.63 eV to 0.69 eV.

It has been reported that the Fermi level in SiC is pinned at the surface (Porter and Davis, 1995). This could be the reason for the significant variation between theoretical and measured values of saturation current density and barrier height. If the Fermi level is pinned, the barrier height will be independent of the metal work function. Additionally, the variations between theory and experiment could be due to a variation in the reported value of electron affinity in SiC and the actual value for our sample.

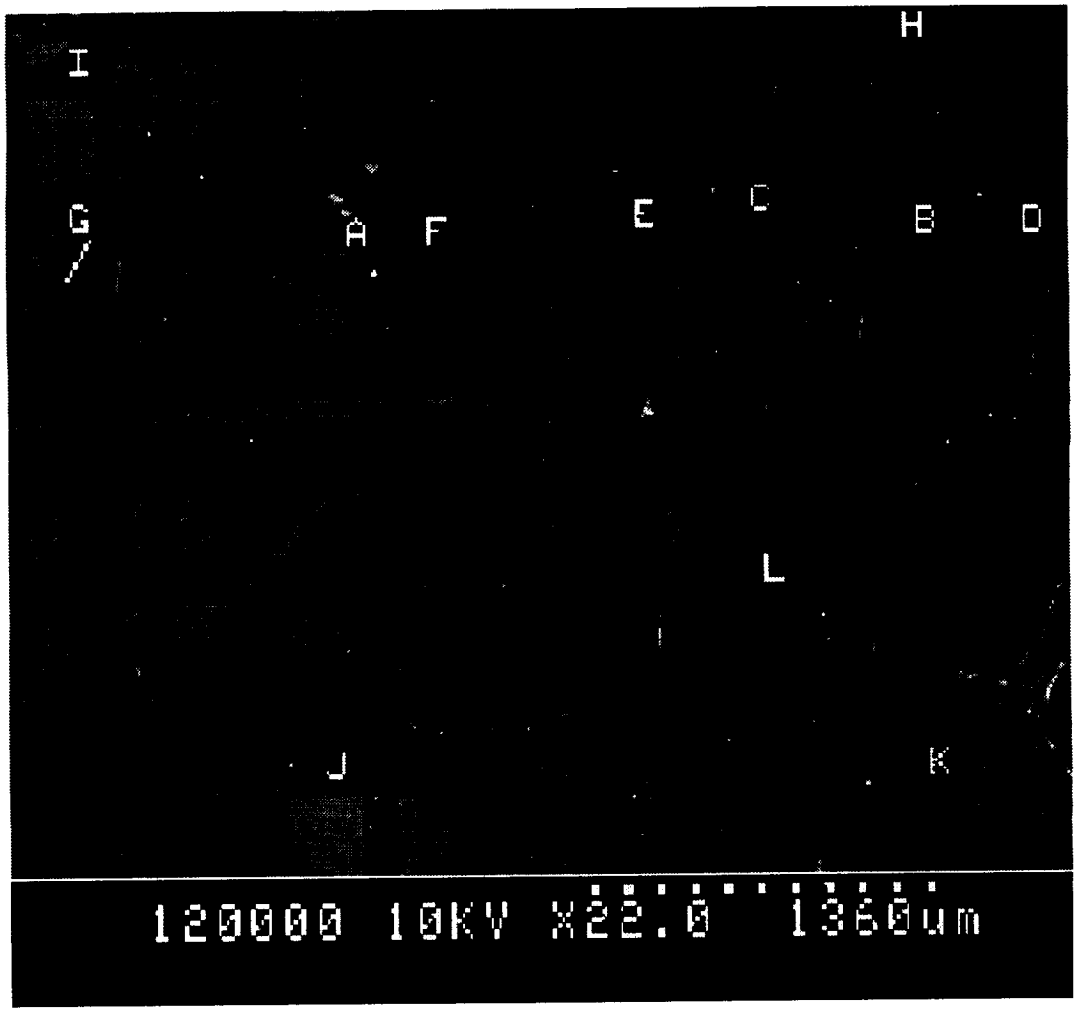

Figure 4.1 Locations of the Sample A diodes used in this study.

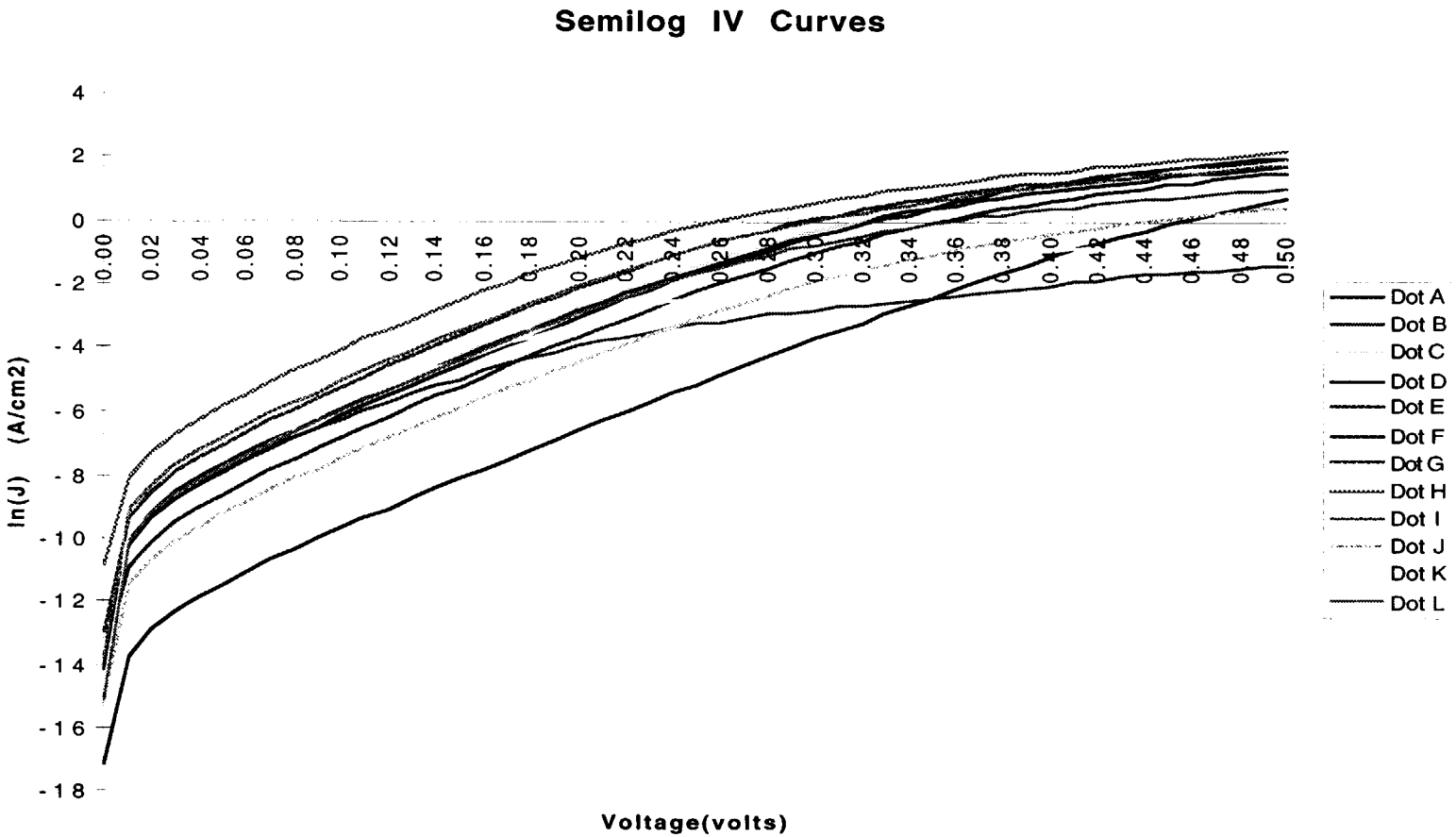

Figure 4.2 Semilog plot of Current Density versus voltage for Dots A-L.

Table 4.1 Results of Experiments on Sample A, Dots A-L

Dot	Carrier Density	Ideality Factor	Saturation Current Density (A/cm^2)	Barrier Height (eV)	Extracted Diffusion Length (μm)	Extracted Metal Thickness (Å)
A1	1.5E+17	1.14	1.68E-04	0.63	0.87	1650
A2					0.78	1604
A3					0.83	1645
B	1.5E+17	1.13	1.51E-04	0.64	0.86	1646
C1	1.5E+17	1.15	1.69E-04	0.63	0.88	1903
C2					0.77	1788
C3					0.85	1798
D	1.6E+17	1.21	9.13E-05	0.65	1.42	1588
E		1.18	4.18E-05	0.67	1.46	1503
F	1.5E+17	1.15	9.47E-05	0.65	0.98	1528
G	2.3E+17	1.12	1.68E-04	0.63	1.04	1522
H		1.15	5.93E-04	0.60	0.87	1629

Dot	Carrier Density	Ideality Factor	Saturation Current	Barrier Height	Extracted Diffusion	Extracted Metal

			Density (A/cm^2)	(eV)	Length (μm)	Thickness (Å)
I	1.4E+17	1.14	2.19E-04	0.63	0.68	1591
J	1.6E+17	1.16	2.03E-05	0.69	0.86	1518
K	1.5E+17	1.21	1.17E-04	0.64	1.02	1551
L	1.2E+17	1.13	8.40E-05	0.65	1.03	1659

In order to measure the doping concentration, we performed CV analysis on all Sample A Dots except Dots E and H. Dots E and H were excluded due to excessive mechanical damage to the metal layer. From this data we extracted a doping concentration using the theory and procedure outlined in Chapters 2 and 3. The doping concentrations are shown in Table 4.1. Plots of $1/C^2$ versus voltage are shown for each dot in Figure 4.3.

Using a value of $1.5*10^{17}$ cm^{-3} for doping and a built in voltage of 0.5 V, a value of 700Å was calculated for depletion layer thickness using Equation 2.14. It has been shown (Wu and Wittry, 1978) that variations in the depletion layer thickness have a very small effect on the collection efficiency. The collection efficiency is much more sensitive to diffusion length and metal layer thickness. Therefore, we feel that the use of an estimated depletion layer thickness in our program is justified.

An EBIC analysis was performed on each contact and a diffusion length and metal layer thickness extracted using the value of depletion layer thickness stated above, a density of SiC of 3.21 g/cm^3, and the density of titanium of 4.5 g/cm^3. Additionally, for Dots A and C, we performed three measurements per dot. The extracted diffusion length and metal layer thickness' are reported in Table 4.1. The EBIC images showing the points where the EBIC data was measured are shown in Figure 4.4 a-l. The curve fits for each point are shown in Appendix C.

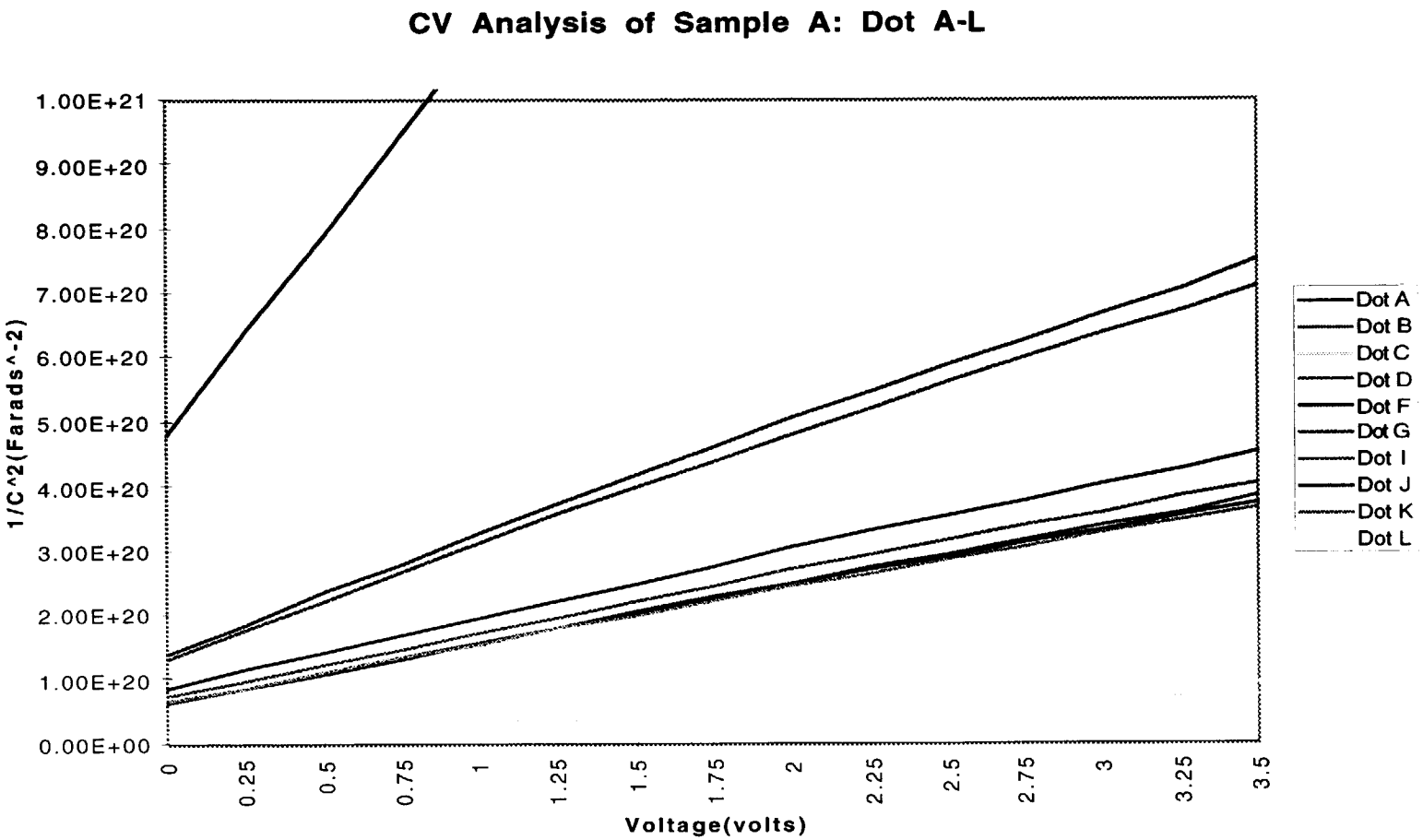

Figure 4.3 Plots of $1/C^2$ vs. V for Dots A-L.

Figure 4.4 a-l) EBIC Images of contacts studied.

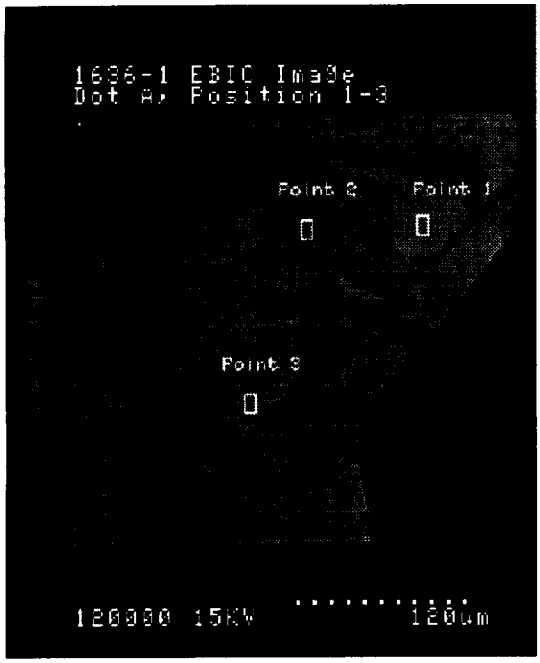

Figure 4.4 a) Dot A EBIC Image

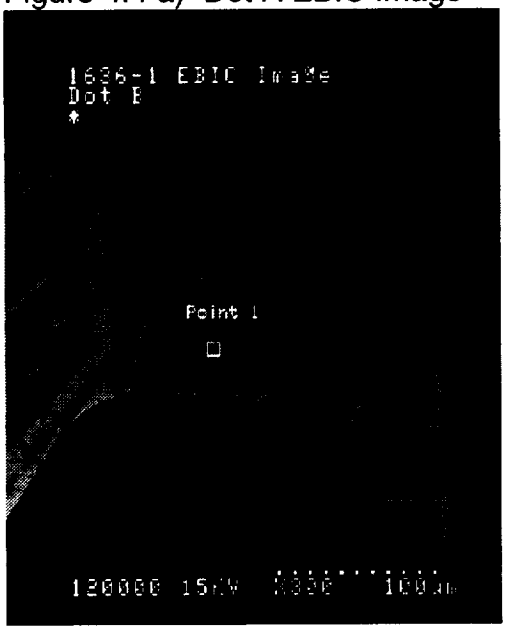

Figure 4.4 b) Dot B EBIC Image

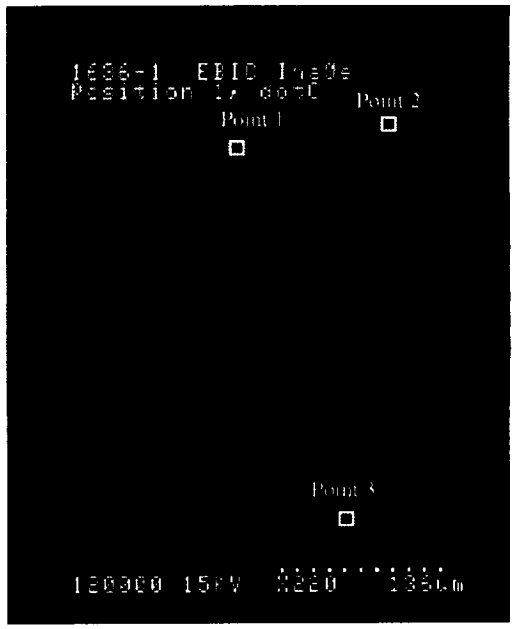

Figure 4.4 c) Dot C EBIC Image

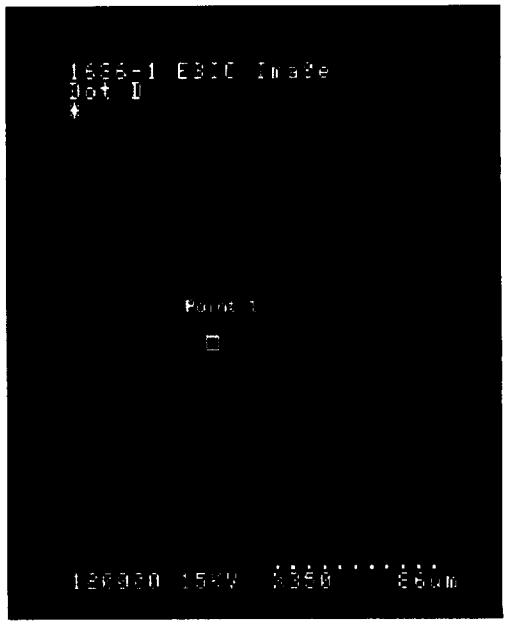

Figure 4.4 d) Dot D EBIC Image

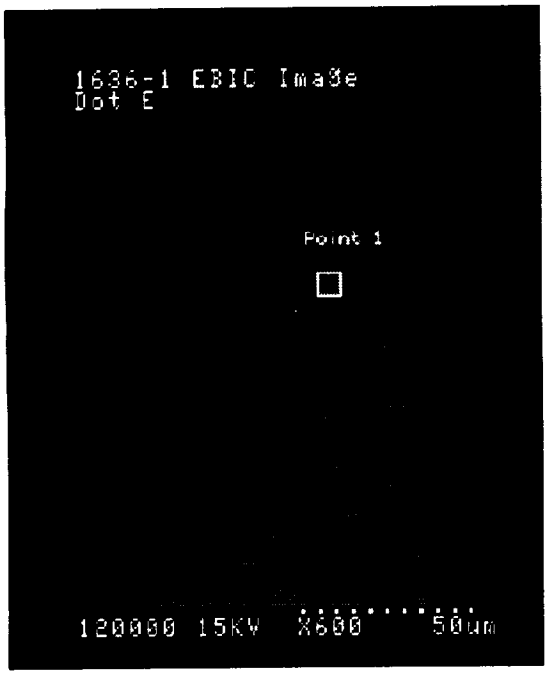

Figure 4.4 e) Dot E EBIC Image

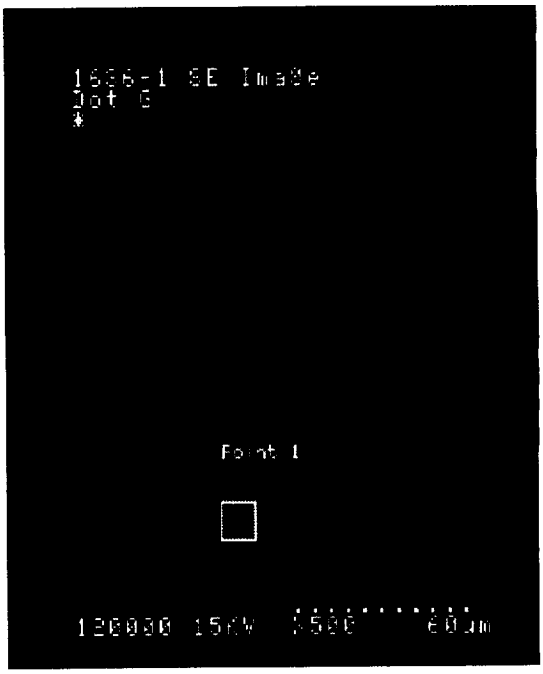

Figure 4.4 g) Dot G EBIC Image

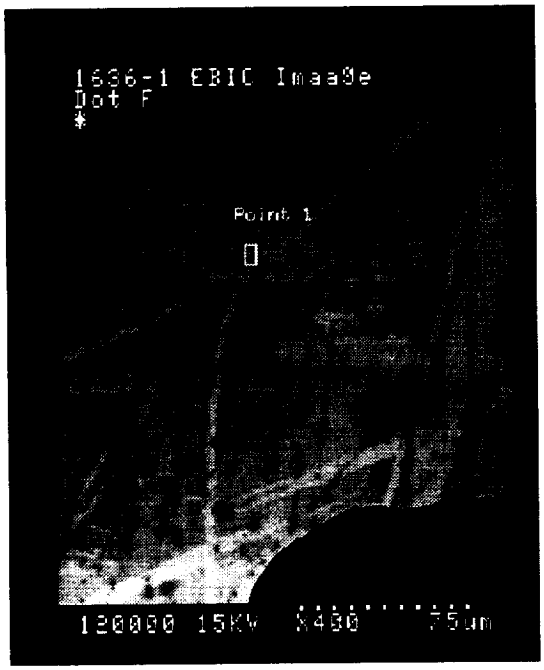

Figure 4.4 f) Dot F EBIC Image

Figure 4.4 h) Dot H EBIC Image

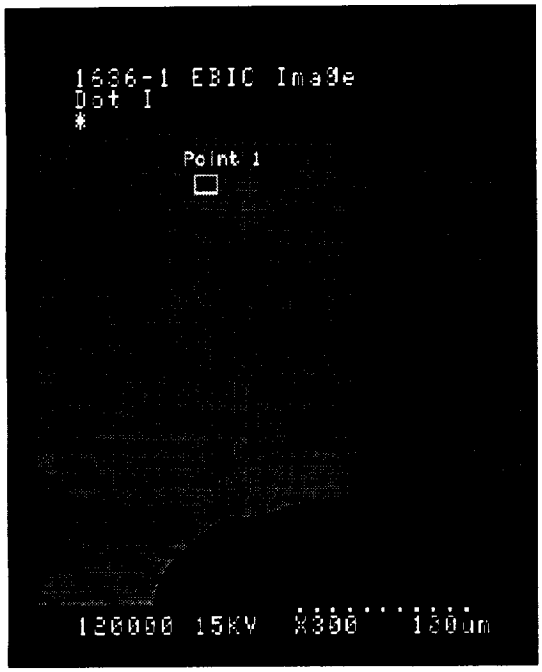

Figure 4.4 i) Dot I EBIC Image

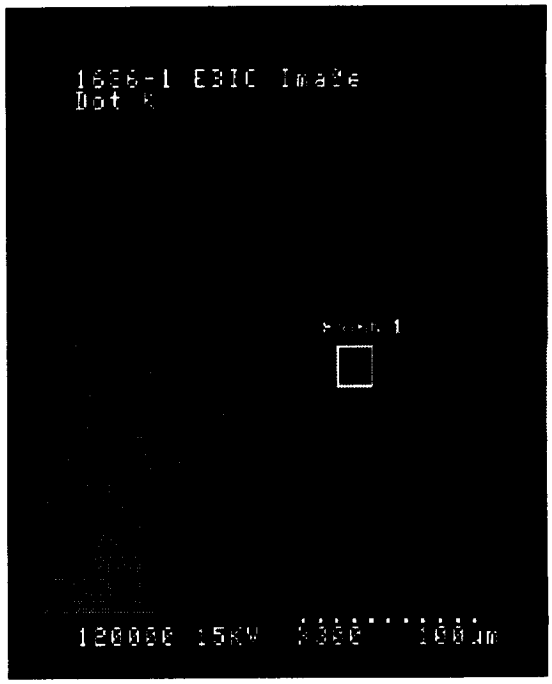

Figure 4.4 k) Dot K EBIC Image

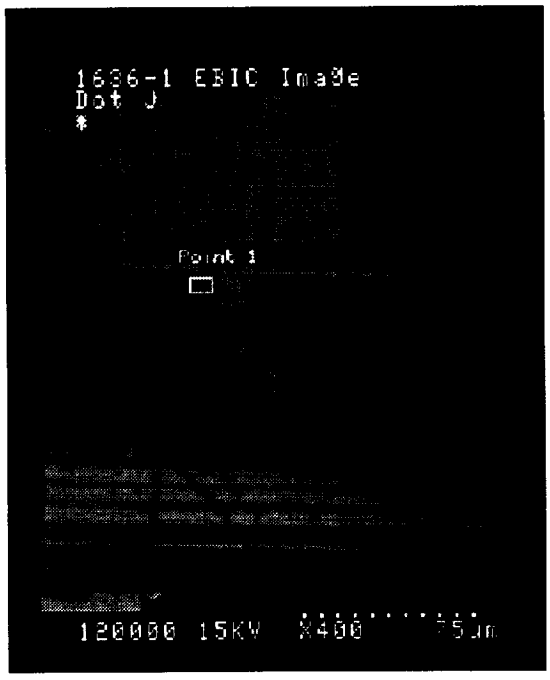

Figure 4.4 j) Dot J EBIC Image

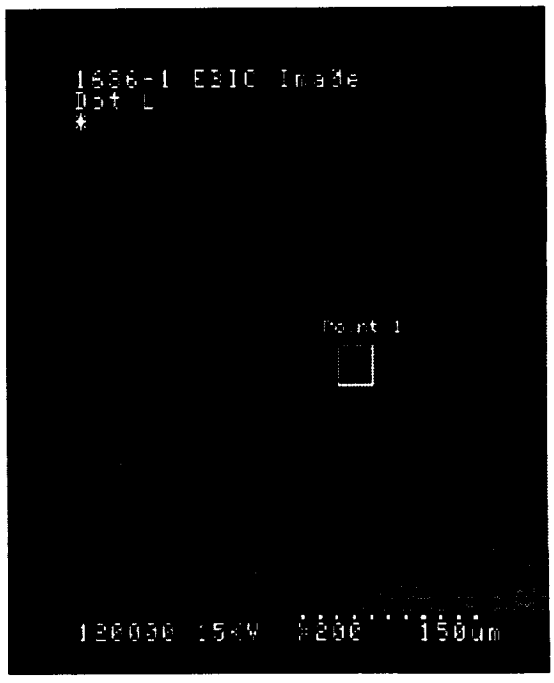

Figure 4.4 l) Dot L EBIC Image

The error for the diffusion length and metal layer thickness was ± 15%. This value is the sum of the nonlinear fit routine error, ±10%, plus an error of ±5% due to variations in the EBIC and beam current. The error due to the fit routine was given as a confidence interval in the output of the fit. The error of 5% was calculated by propagating the maximum and minimum EBIC and Beam Current variations through the fit routine and comparing it to the original value of diffusion length.

Many of the curve fits shown in Appendix C did not reach the maximum theoretical collection efficiency. We believe this is due to the presence of interfacial states. The effect of interfacial states is to reduce the EBIC by causing recombination at the surface. This will in turn reduce the collection efficiency.

Wu and Wittry did not account for interfacial states in there original theory. They assumed that there was 100% collection efficiency in the depletion region. However, in our samples, the presence of interfacial states and recombination in the depletion region violated this "100% depletion region efficiency" assumption resulting in an overestimation of collection efficiency by the Wu and Wittry model. A improved model has been suggested by Tabet and Tarento (1989) in order to account for this effect.

As can be seen from the EBIC images, Sample A had a large defect density. Defects appear as the small black dots in the EBIC images. The shaded areas visible on each dot are due to variations in processing. The wide bright lines are scratches on the metal layer. The scratches will not affect diffusion length, but will reduce the metal layer thickness.

Processing variations across an individual pad will have a very slight effect on extracted diffusion length. This is shown in the results for Dot A1-3 and C1-3. Diffusions lengths extracted on the darker regions are as much as 0.10 μm lower than those on the brighter regions. However, when we consider the ±15% experimental error, the effect of processing variations is insignificant. Results of Dot A and C show that diffusion lengths measured in defect free regions on the same pad remain roughly constant.

Although little variation was seen within the pads, significant variations were seen from pad to pad. This could be due to inhomogenous diffusion length across the sample or processing variations from pad to pad. As processing variations lead to slight changes in diffusion length, we believe that the variation was due to an inhomogenous diffusion length in Sample A.

A very slight correlation between diffusion length and saturation current density was observed. This is expected, as a larger defect density will lead to increased leakage current and a corresponding increase in recombination centers which will drive down the effective bulk diffusion length. Figure 4.5 shows a graph of diffusion length and corresponding saturation current density. In order to arrive at a more statistically meaningful

correlation, many more data points would be necessary in order to account for fluctuation in L.

In order to directly measure the effects of defects on diffusion length we would need a method that allows us to measure diffusion length across the defects seen in the EBIC images. By itself, the planar method does not provide this type of spatial resolution. In order to solve this resolution problem, we propose the planar mapping technique.

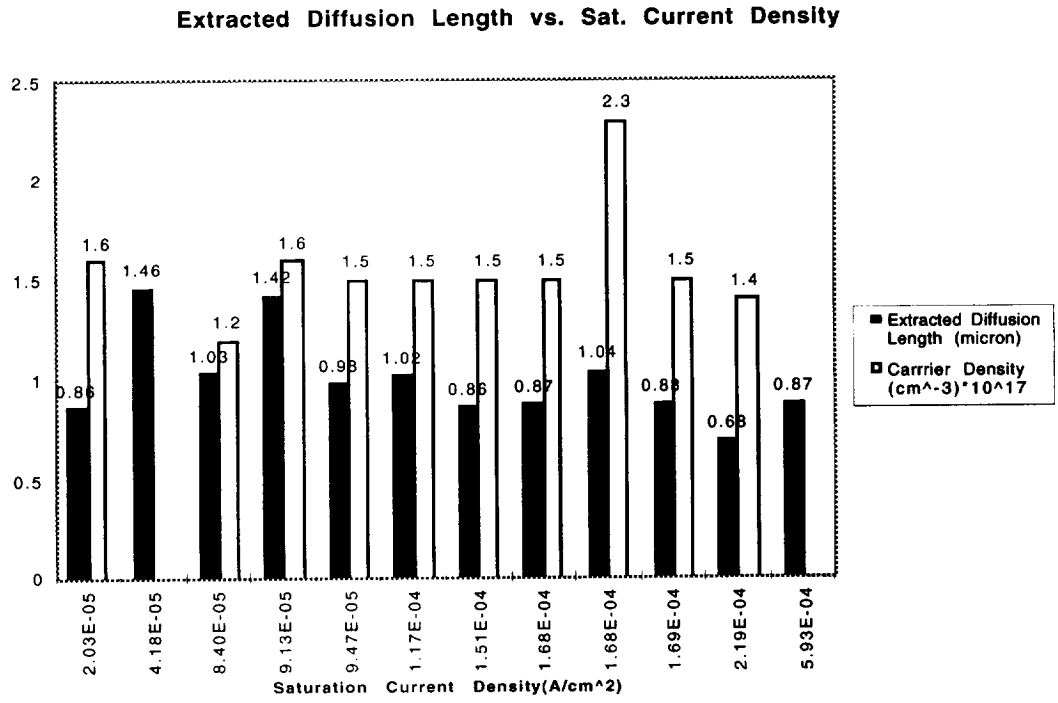

Figure 4.5 Bar Chart of Extracted Diffusion Length vs. Saturation Current Density and Carrier Density.

4.2 Planar Mapping Results

Through the use of computer control and the Wu and Wittry method, we have developed a method to directly visualize the effect of defects on diffusion length. This planar mapping technique was verified on Sample A, Sample C and Sample D. In each case, the planar mapping technique shows that the defects will have the expected effect of reducing the effective bulk minority carrier diffusion length.

Two diffusion length maps were made for Sample A, one on Dot A and one on Dot D. The same depletion layer thickness and densities were uses as in Section 4.1. Figure 4.6a shows diffusion length as a function of beam position for Sample A, Dot A. In Figure 4.6b, we have overlaid 4.6a onto the EBIC image of the linescan. The position and length of the linescan is indicated by the white line. The first 10 points of the linescan were taken off the edge of the contact, and should be disregarded.

Diffusion lengths ranged from near 0.9 μm in defect free regions, to 0.1 μm inside the defects. Figure 4.7 a)-c) shows three representative curve fits, one in a defect free region (at position 25), one near a defect (at position 43), and one inside a defect (at position 57), respectively. Curve fits a) and b) are reasonably accurate fits. However, for fit c) , the accuracy of the fitting routine to the theoretical model has decreased. Inside large defects, the diode efficiency will not be predicted accurately by the Wu and Wittry model. This is most likely due to the assumptions made by the Wu and Wittry model (e.g. 100% collection efficiency in depletion region, no interface states, etc.). Nevertheless, the model does accurately predict the decrease in diffusion length at the center of the defects.

The metal layer thickness remained roughly constant over the linescan. Variations in metal layer thickness were usually less than 100Å, except inside defects, were the model breaks down. Figure 4.8 shows a plot of metal layer thickness versus position.

One of the advantages of this mapping technique is its variable resolution. The resolution of this technique is determined by the number of data points taken and the magnification of the SEM. All of our results are for 100 data points, although this could easily be increased using the Asyst program. However, the Dot D scan illustrates the effect that SEM magnification plays on resolution.

Figure 4.9 shows the diffusion length map for Sample A, Dot D. Curve fits for Dot D can be found in Appendix C. For this experiment, the magnification of the SEM was more than doubled, form X1K for Dot A to X2.2k for Dot D. This had the effect of reducing the distance between beam positions. For Dot A the total scan length, measured from the SEM

micrograph, is 106 μm, giving approximately 1 μm spacing between beam positions. For Dot D, the total scan length is 38.5 μm, giving approximately 0.4 μm beam spacing. Our results for Dot D illustrate the variable resolution of this technique.

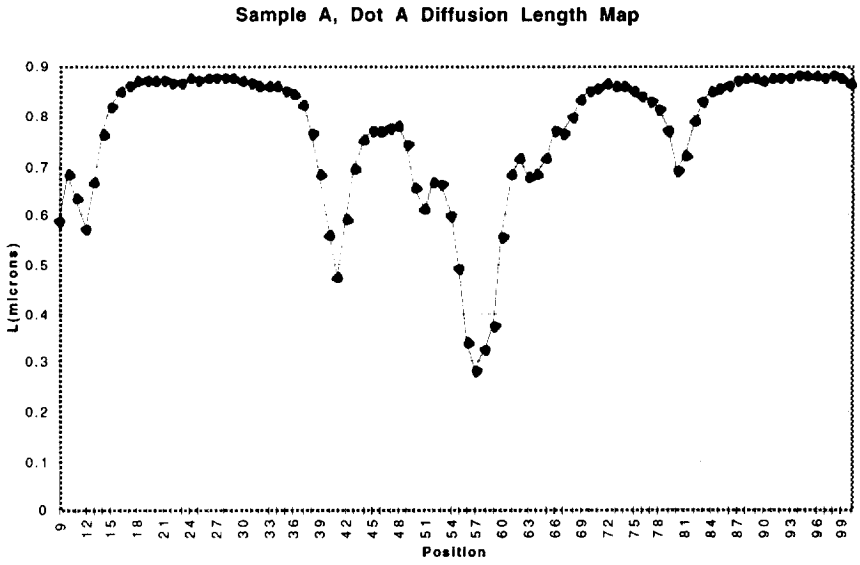

Figure 4.6 a) Hole diffusion length map for Sample A, Dot A.

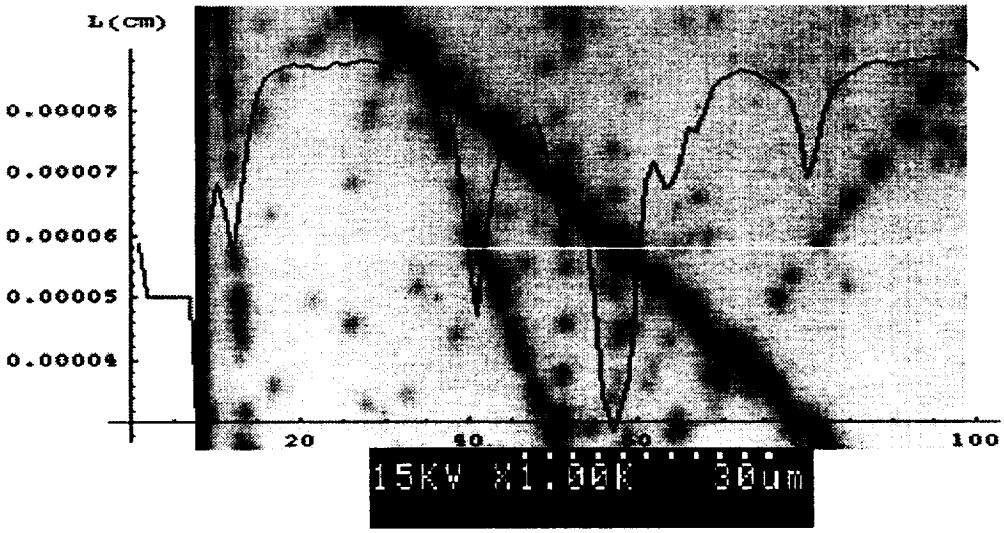

Figure 4.6 b) Diffusion Length Map for Sample A Dot A overlaid onto the EBIC image of the linescan.

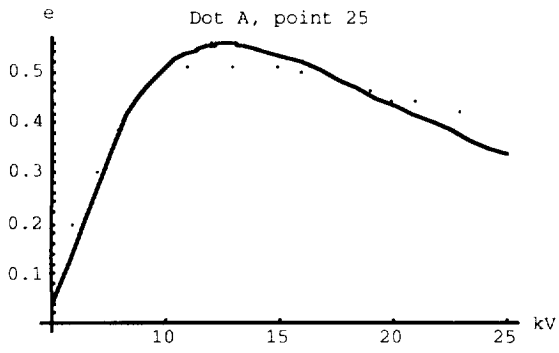

Figure 4.7 a) Curve fit for point 25 of Sample A, Dot A. Data for this fit was taken from a relatively defect free area of the linescan.

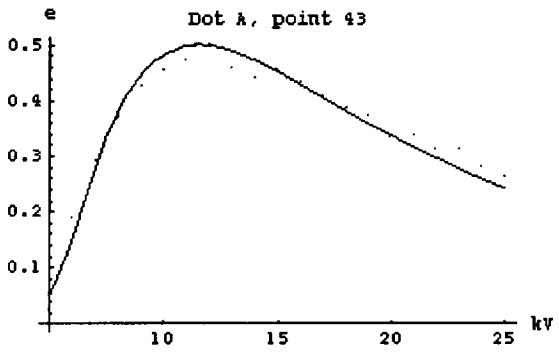

Figure 4.7 b) Curve fit for point 43 of Sample A, Dot A. Data for this fit was taken near a defect.

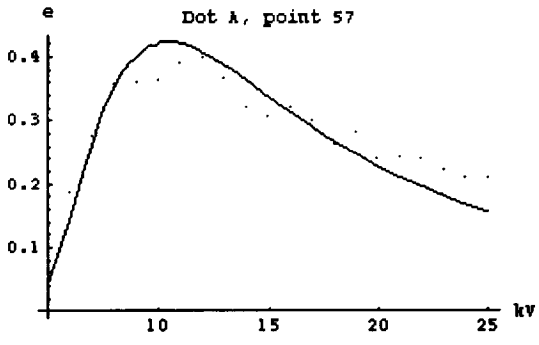

Figure 4.7 c) Curve fit for point 57 of Sample A, Dot A. Data for this fit was taken at the center of a defect.

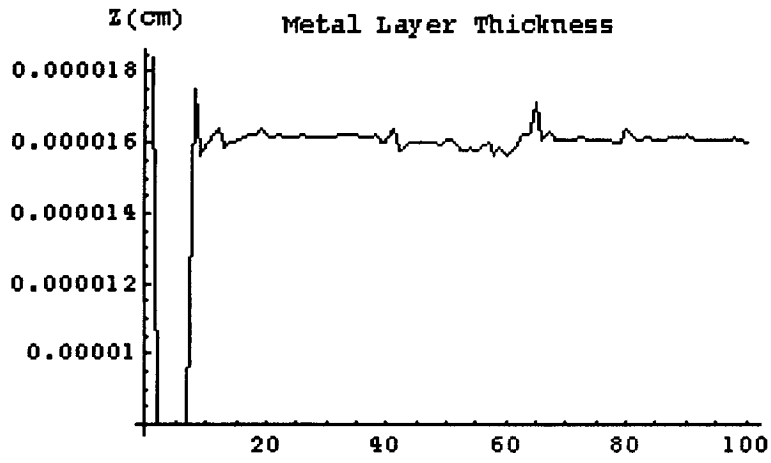

Figure 4.8 Plot of extracted metal layer thickness versus beam position for Sample A, Dot A.

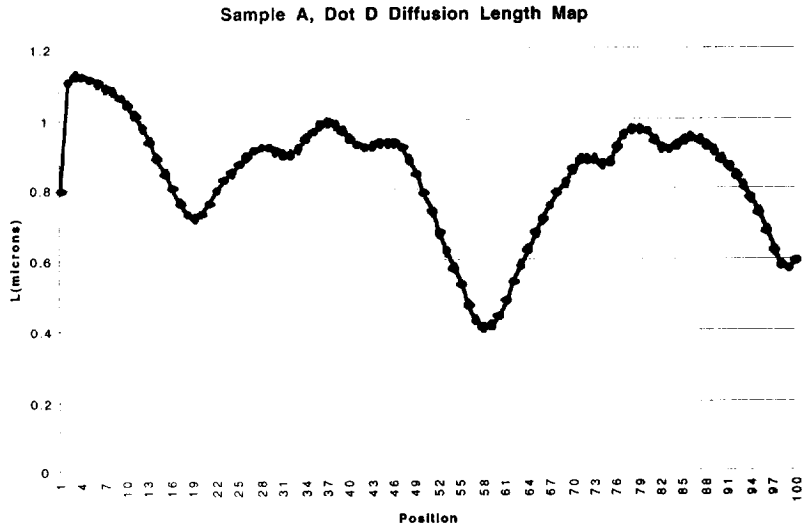

Figure 4.9 a) Hole diffusion length map for Sample A, Dot D.

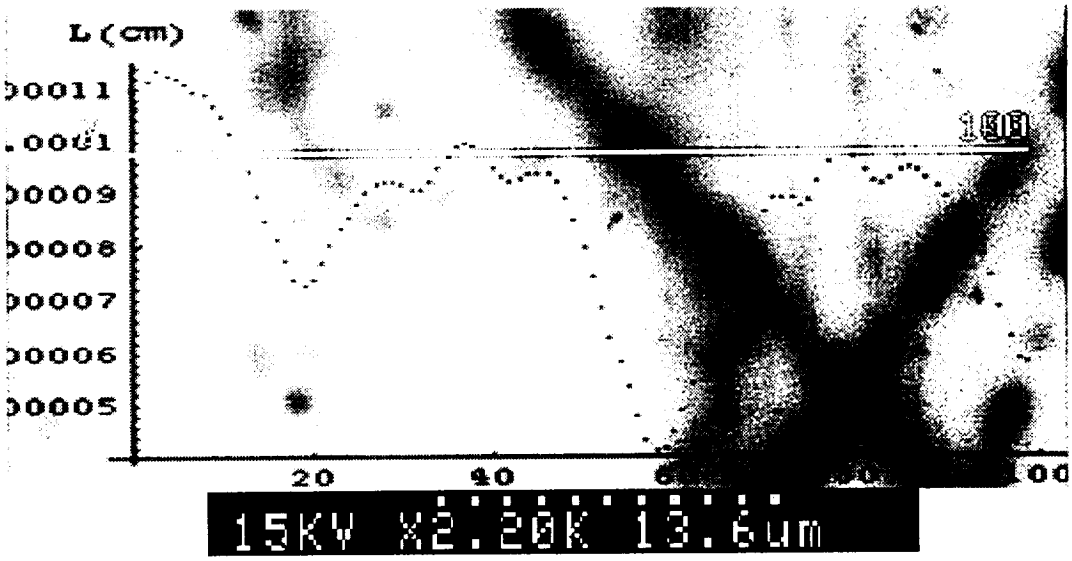

Figure 4.9 b) Diffusion Length Map for Sample A Dot D overlaid onto the EBIC image of the linescan.

A linescan was also taken on Sample C. Sample C used 300Å-400Å of sputter coated Pd as Schottky contacts (Hunter, 1995). The depletion layer thickness was calculated to be 1000Å and a value of 12.4 g/cm^3 was used for the density of palladium. Measurements of IV and CV were also performed on the single 400 μm^2 dot used for our study. The ideality, saturation current density and barrier height were 1.63, 2.69E-14 A/cm^2, and 1.22 eV, respectively. The semilog plot of saturation current density versus voltage is shown in Figure 4.10. The doping concentration of the dot used in our study was 3.42E17 cm^{-3}. Figure 4.11 shows the result of our CV analysis.

Figure 4.12 shows the diffusion length map for Sample C. Appendix C contains curve fits for Sample C. Extracted metal layer thickness for this region was 308Å. Diffusion length ranged from 1.14 μm in the defect free region, to well below 0.1 μm inside the defects.

Figure 4.10 Sample C IV Curve

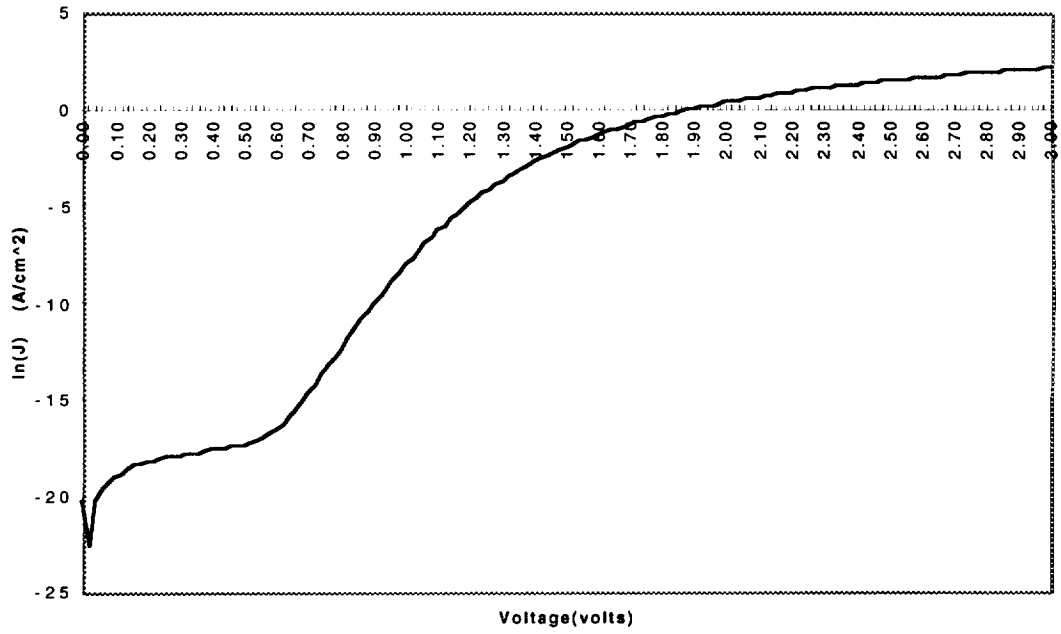

Figure 4.10 Sample C Semilog IV Curve.

Figure 4.11 CV Analysis of Sample C

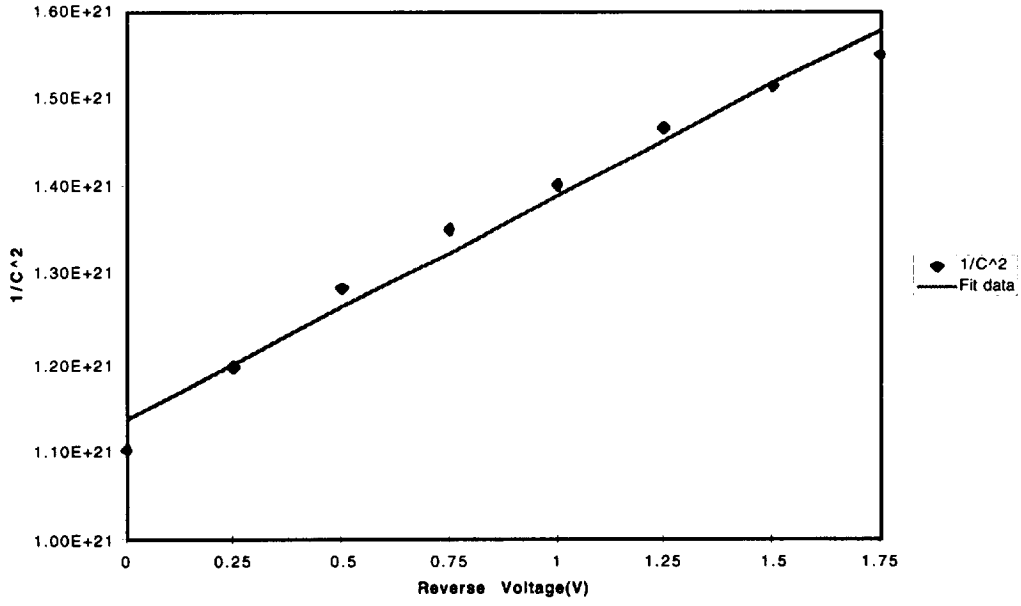

Figure 4.11 CV Analysis of Sample C.

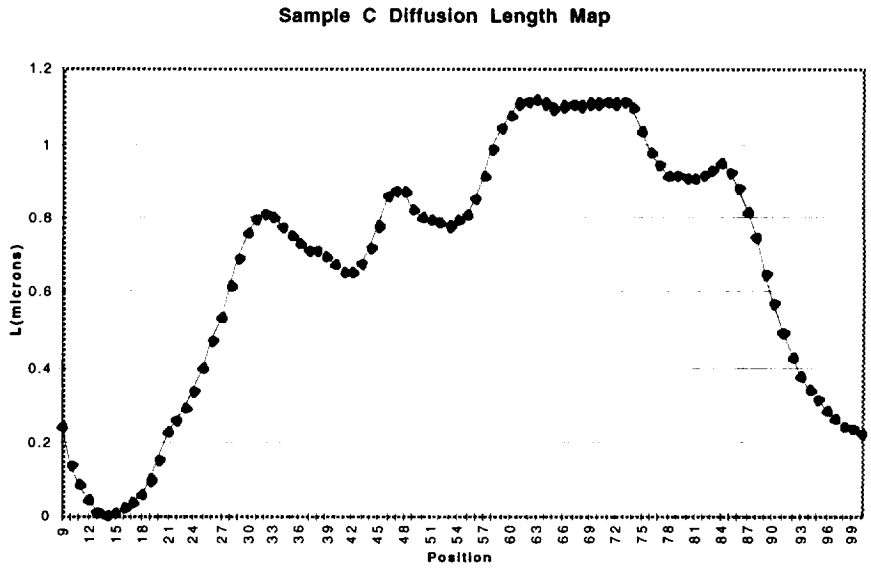

Figure 4.12 a) Hole diffusion length map for Sample C.

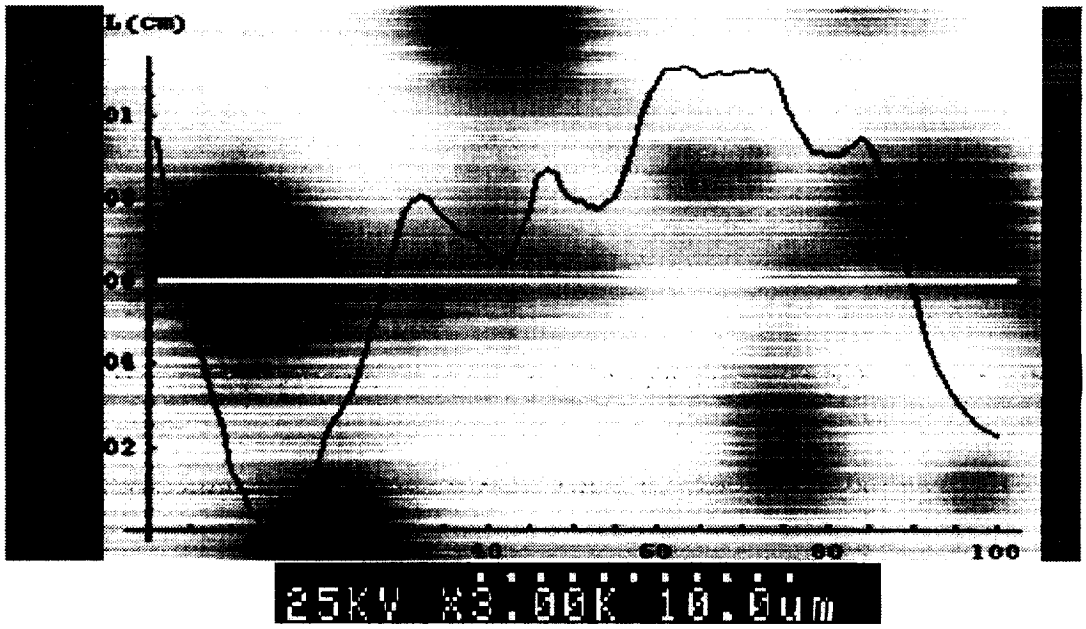

Figure 4.12 b) Diffusion Length Map for Sample C overlaid onto the EBIC image of the linescan.

In order to both measure diffusion length of electrons in p-type SiC, and to illustrate the applicability of the planar mapping technique to the thin n^+ on p geometry, a linescan was performed on Sample D. Prior to the EBIC experiment, IV and CV measurements were performed. The results are shown in Figure 4.13 and 4.14 respectively. The calculated doping concentration for the p side of the junction was 3.3E16 cm^{-3}. A depletion layer thickness of 3000Å was calculated for an abrupt n^+p junction as shown in Sze (1982).

The result of our experiment is shown in Figure 4.15. The diffusion length map was able to accurately show the effect on diffusion length of the two micropipe defects in the image. The extracted metal layer thickness for our entire plot remained roughly constant, ranging from 1190Å to 1170Å. Electron diffusion length for this sample ranged from 1.42 μm to 0.8 μm.

Chapter V: Conclusion

In this thesis we have reported two important results. First, we have measured a fundamental material characteristic in 6H SiC, the minority carrier diffusion length. Second, we have demonstrated a novel EBIC planar mapping method, which allows direct visualization of the effect of defects on minority carrier diffusion length.

In measuring diffusion length, we have reported minority carrier diffusion lengths in both n and p type 6H SiC. Using the planar EBIC method, hole diffusion lengths in defect free regions of n type 6H SiC, with a doping concentration of 1.5E17 cm^{-3}, ranged from 1.46 μm to 0.68 μm. In addition, using the planar mapping technique, we have shown that large defects in SiC severely limit the diffusion length, reducing it below 0.1 μm. Measurements of p-type SiC, with a doping concentration of 3.3E16 cm^{-3}, resulted in values of electron diffusion length ranging from 1.42 μm to 0.8 μm.

The second part of this thesis describes the use of a novel planar mapping technique to directly visualize the effect of defects on diffusion lengths in 6H SiC. We have applied this method to three samples, our original 6H SiC sample, a 6H SiC using very thin Pd contacts, and a commercial diode with a thin n^+ on p geometry. In each case, our technique was able to accurately show the effect of the defects on diffusion length. The resulting map of diffusion length was overlaid onto the EBIC image of the linescan in order to directly visualize this effect.

Additionally, this technique allows us to quantify the effects of individual defects. The effect of each individual defect on diffusion length is shown in the diffusion length map. Using the diffusion length map, we can pinpoint those defects having the most effect on diffusion length.

Due to the interest in SiC as a high temperature semiconductor, we believe the next direction to take in diffusion length measurements of SiC is the use of the planar or planar mapping technique to study the minority carrier diffusion length as a function of temperature. This can be easily accomplished by adding a heating stage to the S-800 SEM. This would allow measurement of diffusion length up to temperatures of 1500° C.

Additionally, a detailed study of diffusion lengths versus doping concentration is needed in 6H, 4H and 3C SiC polytypes. The difficulty in this study lies in the variable defect concentrations typical of SiC. The variable defect density adds another factor into the study and makes comparison of diffusion length and doping unreliable as both doping and defects can have a significant effect on diffusion length.

Chapter VI: References

Acheson, A.G., Engl. Pat. 17911(1892).

Anikin, M.M., Lebedev, A.A., Pyatko, S.N., Soloviev, V.A., Strelchuk, A.M., In Springer Proc. in Physics vol. 56: Amorphous and Crystalline Silicon Carbide III, (Harris, G.L., Spencer, M.G., Yang, C.Y. Editors, Springer Verlag, Berlin, 1992) p269-273.

Babcock, R., IEEE Trans. on Nuclear Science NS-10, p43-47(1965).

Balona, L.A., Loubser, J.H.N., J. Phys. C: Solid St. Phys. 3, p2344-2351(1970).

Barrett, D.L., Seidensticker, R.G., Hopkins, R.H., Choyke, W.J., J. of Cryst. Growth 109, P17-23(1991).

Barry, A.L., Lehmann, B., Fritsch, D., Braunig, D., IEEE Trans. on Nuclear Science 38, p1111-1115(1991).

Bishop, H.E., Ph.D. Dissertation (Cambridge, 1966).

Brown, D.M., Downey, E.T., Ghezzo, M., Kretchmer, W., Saia, R.J., Yung, S.L., Edmond, J.A., Gati, G., Pimbley, J.M., Schneider, W.E., IEEE Trans. Electron Dev., 40, p325-333(1993).

Carter, C.H., Tang, L., Davis, R.F., presented at Fourth National Review Meeting on the Growth and Characterization of SiC, (Raleigh, NC, 1987).

Chan, D.S.H., Ong, V.K.S., Phang, C.H., IEEE Trans. on Electron Dev. 42, p963-968(1995).

Donalato, C., Solid State Electronics 25, p1077-1081(1982).

Ehrenberg, W., Gibbons, D.J., Electron Bombardment Induced Conductivity and Its Applications, (Academic Press, London, 1981).

Everhart, T.E., Hoff, P.H., J. Appl. Phys. 42, p5837-46(1971).

Goldstein, J.I., Newbury, D.E., Echlin, P., Joy, D.C., Fiori, C., Lifshin, E., Scanning Electron Microscopy and X-ray Microanalysis, (Plenum Press, New York, 1984).

Gruen, A.E., Z. Naturforsch. 12A, p89-95(1956).

Hart, R.R., Dunlap, H.L., Marsh, O.J., Radiation Effects 9, 261-266(1971).

Heine, V., Chang, C., Engel, G.E., Needs, R.J., In: Wide Bandgap Semiconductors, Proc. Materials Research Society, Ed. Moustakas, T.D., Pankove, J.I., Hamakawa, Y., p507-518, (Materials Research Society, Pittsburgh 1991).

Heinrich, K.F.J. X-Ray Optics and Microanalysis, 4th Intl. Conf. on X-Ray Optics and Microanalysis, Eds. Castaing, R. Deschamps, P., Philibert, J., (Hermann, Paris 1966).

Holt, D.B., Joy, D.C., SEM Microcharacterization of Semiconductors, (Academic Press, London, 1989).

Honstvet, I.A., Smallman, R.E., Marquis, P.M., Phil. Mag. 41, p201-207(1980).

Hunter, G.W., Neudeck, P.G., Chen L.-Y., Knight, D., Liu, C.C., Wu, Q.H., American Institute of Aeronautics and Astronautics Paper #95-2647 (AIAA, Washington, D.C. 1995).

Ioannou, D.E., Dimitriadis, C.A., IEEE Trans. on Electron Dev. 29, p445-450(1982).

Itoh, H., Yoshikawa, M., Nashiyama, S., Misawa, S., Okumura, H., Yoshida, S.,IEEE Trans. on Nuclear Science 37, p1732-1738(1990).

Kanaya, T.E., Okayama, S., J. Phys. D: Appl. Phys. 5, p43-58(1972).

Klein, C.A., J. Appl. Phys. 39, p2029-2038(1968).

Knippenberg, W. F., Philips Res. Repts. 18, 161-274(1963).

Kyser, D.F., Proc. of the 6th Int. Conf. on x-ray Optics and Microanalysis, (University of Tokyo Press, Tokyo, 1972), p147.

Larkin, D.J., Neudeck, P.G., Powell, J.A., Matus, L.G., Appl. Phys. Lett. 65, p1659-1661(1994).

Leamy, H.J., J. Appl. Phys. 53, pR51-R78(1982).

Michalson, H.B. Handbook of Chemistry and Physics, Work Functions of the Elements (58th Ed., CRC Press, Cleveland, OH, 1978) pE81-E82.

Moissan, H., C.R. Acad. Sci. Paris 140, 405(1905).

Morkoc, H., Strite, S., Gao, G.B., Lin, M.E., Sverdlov, B. Burns, M., J. Appl. Phys. 76, 1363-1398(1994).

Moustakas, T.D., Pankove, J.I., Hamakawa, Y., Materials Research Society Symposium Proceedings: Wide Band Gap Semiconductors, vol 242, (Materials Research Society, Pittsburgh 1991).

Nakashima, S., Institute of Physics Conference Series Number 142: Silicon Carbide and Related Materials, (Institute of Physics Publishing, Bristol 1995).

Neudeck, P., "Recent Progress in Silicon Carbide Semiconductor Electronics Technology", (at: http://www.lerc.nasa.gov/WWW/ SiC/SiCReview.html, 1997).

Neudeck, P.G., Larkin, D.J., Powell, J.A., Matus, L.G., Salupo, C.S., Appl. Phys. Lett. 64, p1386-1388(1994a).

Neudeck, P.G., Larkin, D.J., Starr, J.E., Powell, A., Salupo, C.S., Matus, L.G., IEEE Elect. Dev. Lett. 14, p136-139(1993).

Neudeck, P.G., Larkin, D.J., Starr, J.E., Powell, A., Salupo, C.S., Matus, L.G., IEEE Trans. on Electron Dev. 41, p826-835(1994b).

Neudeck, P.G., Powell, J.A., IEEE Elect. Dev. Lett. 15, p63-65(1994c).

Pensl, G., Choyke, W.J., Physica B 185, p264-283(1993).

Pirouz, P., Yang, J.W., Ultramicroscopy 51, 189-214(1993).

Porter, L.M., Davis, R.F., Mat. Sci. and Eng.:B B34, p83-105(1995).

Powell, J.A., Larkin, D.J., Matus, L.G., Choyke, W.J., Bradshaw, J.L., Handerson, L., Yoganathan, M., Yang, J. Pirouz, P., Appl. Phys. Lett. 56, 1353-1355(1990).

Powell, J.A., Neudeck, P.G., Matus, L.G., Petit, J.B., In: Wide Bandgap Semiconductors, Proc. Materials Research Society, Ed. Moustakas, T.D., Pankove, J.I., Hamakawa, Y., p495-505,(Materials Research Society, Pittsburgh 1991).

Press, W.H., Flannery, B.P., Teukolsky, S.A., Vetterling, W.T., Numerical Recipes: The Art of Scientific Computing, (Cambridge Univ. Press, Cambridge, 1989).

Reuter, W. In Proc. 6th Intl. Conf. X-Ray Optics and Microanalysis, Eds. Shinoda, G., Kohra, K., Ichinokawa, T., (University of Tokyo Press, Tokyo, 1972), p121.

Sharma, B.L., Metal-Semiconductor Schottky Barrier Junctions and their Applications, (Plenum Press, New York, 1984).

Spencer, M.G., Devaty, R.P., Edmond, J.A., Asif Khan, R. Rahman, M., Institute of Physics Conference Series Number 137: Silicon Carbide and Related Materials, (Institute of Physics Publishing, Bristol 1993).

Sternglass, E.J., Phys. Rev. 95, p345(1954).

Stevenson, D.T., Keyes, R.J., J. Appl. Phys. 26, p835(1955).

Streetman, B.G., Solid State Electronic Devices, (4th Ed., Prentice Hall, New Jersey, 1995).

Sze, S.M., Physics of Semiconductor Devices, (2nd ed., Wiley-Interscience, New York, 1981).

Tabet, N., Tarento, R., Phil. Mag. B 59, p243-261(1989).

Tairov, Y.M., Tsvetkov, V.F., J. Cryst. Growth 43, 209(1978).

Tairov, Y.M., Tsvetkov, V.F., J. Cryst. Growth 52, 146(1981).

Wittry, D.B., Kyser, D.F., J. Appl. Phys. 38, p375(1967).

Wu, C.J., Wittry, D.B., J. Appl. Phys. 49, p2827-2836(1978).

Yang, J. W., Ph.D. Dissertation, Case Western Reserve University, Cleveland, OH(1993).

Yang, J.W., Suzuki, T., Pirouz, P., Powell, J.A., Iseki, T., In: Wide Bandgap Semiconductors, Proc. Materials Research Society, Ed. Moustakas, T.D., Pankove, J.I., Hamakawa, Y., p531-542,(Materials Research Society, Pittsburgh 1991).